

Constraining the Interiors of Asteroids Through Close Encounters

Jack T. Dinsmore,^{1*} Julien de Wit²

¹*Department of Physics, Massachusetts Institute of Technology*

²*Department of Earth, Atmospheric, and Planetary Science, Massachusetts Institute of Technology*

Accepted XXX. Received YYY; in original form ZZZ

ABSTRACT

Knowledge of the interior density distribution of an asteroid can reveal its composition and constrain its evolutionary history. However, most asteroid observational techniques are not sensitive to interior properties. We investigate the interior constraints accessible through monitoring variations in angular velocity during a close encounter. We derive the equations of motion for a rigid asteroid’s orientation and angular velocity to arbitrary order and use them to generate synthetic angular velocity data for a representative asteroid on a close Earth encounter. Using Markov Chain Monte Carlo fits, we perform injection-retrieval tests on these synthetic data to gain insights into the extent to which interior properties can be constrained. We also perform a sensitivity analysis of such an inversion technique to asteroid parameters (e.g., moment of inertia and initial spin pole direction), observational set-up (e.g., measurement precision and cadence), and mapping models to convert constraints on the density moments to density distributions. We find that high precision in rotational period estimates (order of milliseconds to seconds) are necessary for each cadence, and that large asteroids (> 100 m radius) with low perigees (< 20 Earth radii) are necessary to resolve second-order density moments.

Key words: minor planets, asteroids: general – methods: data analysis

1 INTRODUCTION

Over the past twenty years, the increase in quantity and quality of sensitive all-sky surveys has prompted the discovery of numerous asteroids. Such advances have been made via ground-based surveys such as the Catalina Sky Survey [Larson et al. \(1998\)](#), Pan-STARRS [Kaiser et al. \(2002\)](#), and the Lincoln Near-Earth Asteroid Research project (LINEAR) [Stokes et al. \(2000\)](#), as well as space-based instruments such as the Wide-field Infrared Survey Explorer (WISE) mission [Wright et al. \(2010\)](#). Many of these asteroids are relatively small, but some are kilometre-sized and a few are predicted to closely encounter Earth or other planets in the near future. More encounter candidates are likely to be discovered by new efforts such as the Large-aperture Synoptic Survey Telescope (LSST) [Tyson \(2002\)](#). Their encounters can then be monitored by global ground-based networks such as the Las Cumbres Observatory (LCO) [Brown et al. \(2013\)](#). Such ground-based monitoring is typically used to derive the rotation period of an asteroid and its surface properties (see e.g. [Devogèle et al. \(2021\)](#)).

Since the tidal torque acting on an asteroid during an

encounter depends on the interior mass distribution, the careful monitoring of angular velocity variations during an encounter also presents a window into the interior properties of asteroids. The gravitational two-body system has been studied in the context of tidal torque to different orders and with several different methods [Paul \(1988\)](#); [Scheeres et al. \(2000\)](#); [Ashenbergs \(2007\)](#); [Boué & Laskar \(2009\)](#); [Hou et al. \(2017\)](#). Further studies showed that the tidal torque, observed through angular velocity perturbations, is sensitive to asteroid interior density distribution [Naidu & Margot \(2015\)](#); [Makarov et al. \(2022\)](#); [Scheeres et al. \(2004\)](#). However, density distribution features beyond the moment of inertia (MOI) ratios have not yet been extracted for any asteroid encounters. More research is needed to study in what cases these effects are observable, and what factors generally inhibit observation of these new features.

Angular velocity perturbations have been observed and used to extract asteroid properties in several cases, including for the 2013 encounter of (367943) Duende with Earth [Moskovitz et al. \(2020\)](#); [Benson et al. \(2020\)](#), and asteroid binaries (3905) Doppler and (617) Patroclus [Descamps et al. \(2020\)](#); [Berthier et al. \(2020\)](#). Orbital and physical properties, including MOI ratios have also been extracted for 99942 Apophis, which will closely encounter Earth in 2029 [Yu et al. \(2019\)](#).

* E-mail: jtdinsmo@mit.edu

(2014); Hirabayashi et al. (2021); Valvano et al. (2022); Lee et al. (2022). It seems pivotal to augment previous work on the affect of tidal torque on Apophis’ angular velocity Souchay et al. (2014, 2018) so that upcoming observations may constrain these properties and thus improve our predictions.

We address this community need by developing a methodology to translate (1) time series of asteroid angular velocity data into constraints on density moments and (2) constraints on density moments into constraints on an asteroid’s density distribution. Other techniques, such as measurement of tidal distortion Richardson et al. (1998), impact or seismometry experiments Richardson et al. (2005), or gradiometry Carroll & Faber (2018), may additionally constrain the density distribution. In section 2, we introduce the analytical and numerical fundamentals of this methodology. There, we describe a simulation used to integrate the equations of motion and produce synthetic data of angular velocity over time, followed by a Markov Chain Monte Carlo (MCMC) fit process which extracts density moments from the fit data. We note that these equations of motion for an asteroid equation are novel and designed to be computationally efficient and valid to arbitrary order. We then describe three methods to generate full density distributions from the density moments. In section 3, we present the results of a series of injection-retrieval tests demonstrating the extent to which the properties of an asteroid chosen to generate synthetic spin data can be retrieved via our methodology. Finally, in section 4, we assess the sensitivity of these constraints to various physical, observational, and methodological parameters to provide guidance for monitoring upcoming close encounters. We also test the density distribution extraction methods on several sample asteroids.

2 METHODS

The only properties of an asteroid’s density moments that affect tidal torque interactions are its “density moments,” defined here as

$$K_{\ell m} = \frac{a_{\mathcal{A}}^{2-\ell}}{I_{\mathcal{A}}} \int_{\mathcal{A}} d^3 r \rho_{\mathcal{A}}(\mathbf{r}) R_{\ell m}(\mathbf{r}). \quad (1)$$

These are complex, unitless quantities. $\rho_{\mathcal{A}}(\mathbf{r})$ is the asteroid density distribution and $R_{\ell m}$ are the regular solid spherical harmonics (see appendix A for details). The integral is computed over the entire asteroid mass, denoted \mathcal{A} . $I_{\mathcal{A}}$ denotes a MOI scale defined as

$$I_{\mathcal{A}} = \int_{\mathcal{A}} d^3 r \rho_{\mathcal{A}}(\mathbf{r}) r^2 \quad (2)$$

while $a_{\mathcal{A}}$ is the length scale

$$a_{\mathcal{A}}^2 = \frac{1}{V_{\mathcal{A}}} \int_{\mathcal{A}} d^3 r r^2 \quad (3)$$

where $V_{\mathcal{A}}$ is the asteroid volume. We call these MOI and length scales in part because they obey $I_{\mathcal{A}} = \mu_{\mathcal{A}} a_{\mathcal{A}}^2$ where $\mu_{\mathcal{A}}$ is the mass of the asteroid for uniform asteroids. Note that $a_{\mathcal{A}}$ is a function only of the surface of the asteroid, so that $a_{\mathcal{A}}$ is known if the surface is observed.

The tidal torque experienced by an asteroid is

$$\begin{aligned} \tau = & G \frac{\mu_{\mathcal{B}}}{2} \left[I_{\mathcal{A}} \sum_{\ell m} a_{\mathcal{B}}^{\ell} J_{\ell m} \sum_{\ell' m'} a_{\text{surf}}^{\ell'-2} S_{\ell+\ell', m+m'}^*(\mathbf{D}) (-1)^{\ell'} \right. \\ & \times \sum_{m''=-\ell'}^{\ell'} \sqrt{\frac{(\ell' - m'')! (\ell' + m'')!}{(\ell' - m')! (\ell' + m')!}} \mathcal{D}_{m' m''}^{\ell'}(\alpha, \beta, \gamma)^* \\ & \times \left. (i\hat{\mathbf{x}} - \hat{\mathbf{y}})(\ell' - m'' + 1) K_{\ell', m''-1} \right. \\ & \left. + (i\hat{\mathbf{x}} + \hat{\mathbf{y}})(\ell' + m'' + 1) K_{\ell', m''+1} + 2im'' \hat{\mathbf{z}} K_{\ell' m''} \right], \end{aligned} \quad (4)$$

where \mathbf{D} is the position of the asteroid; α , β , and γ are $z - y - z$ Euler angles expressing the orientation of the asteroid; $S_{\ell m}$ are the irregular solid spherical harmonics; and $\mu_{\mathcal{B}}$ and $a_{\mathcal{B}}$ are the mass and radius of the central body while $J_{\ell m}$ are the density moments of the central body, with the a_{bulk} and a_{surf} of equation 1 replaced by $a_{\mathcal{B}}$. Equation 4 is derived in appendix A, assuming a rigid asteroid and no third-body perturbations.

Since it is the angular acceleration of the asteroid that is observable, rather than the torque applied, we also compute the MOI of the asteroid around the principal axes:

$$\begin{aligned} I_x &= \frac{2}{3} I_{\mathcal{A}} (K_{20} - 6K_{22} + 1) \\ I_y &= \frac{2}{3} I_{\mathcal{A}} (K_{20} + 6K_{22} + 1) \\ I_z &= \frac{2}{3} I_{\mathcal{A}} (-2K_{20} + 1). \end{aligned} \quad (5)$$

The angular acceleration of the asteroid is proportional to τ/I (equation A14), such that the $I_{\mathcal{A}}$ factor of equation 4 is canceled out. Thus, the observables do not depend explicitly on $I_{\mathcal{A}}$, nor on the asteroid mass.

Throughout the paper, we refer to the “inertial frame” (the frame in which the orbit is fixed) and the “body-fixed frame” (the frame in which the asteroid is fixed), which are also defined in appendix A.

2.1 Simulation design

We built a publicly accessible, custom simulation in C++ to produce time series of angular velocity data during a close encounter with a central body. This simulation requires as initial data (1) the orbital parameters of the asteroid r_p (perigee distance) and v_{∞} (hyperbolic excess velocity); (2) the cadence of angular velocity observation Δt ; (3) the central body moments $J_{\ell m}$, mass $\mu_{\mathcal{B}}$, and radius $a_{\mathcal{B}}$; (4) the initial asteroid angular velocity in the inertial frame Ω_0 ; (5) the asteroid length $a_{\mathcal{A}}$ and (6) the asteroid’s density moments $K_{\ell m}$ and initial Euler angle γ_0 . All parameters except (6) are assumed to be known to high accuracy. For example, Ω_0 could be extracted from pre-encounter light-curve data and a_{surf} from a model for the asteroid’s surface using radar.

We assume for simplicity that the asteroid is initially not tumbling, though this assumption can be relaxed. We assume a short-axis rotation mode such that energy of the asteroid’s rotation is minimized. This sets $\beta = 0$ and we can further choose $\alpha = 0$. Only the Euler angle γ_0 is necessary to provide initial data for the simulation.

We begin our simulation at $D = 10r_p$, with velocity predicted by Kepler's laws given by the orbital parameters. Since the leading order of the equations of motion is $\ell' = 2, \ell = 0$, this corresponds roughly to a torque of 10^{-3} times the maximum torque at perigee. Unless otherwise indicated, the simulation is terminated at $D = 10r_p$ as well.

With the simulation inputs specified, the equations of motion are integrated via the Runge-Kutta fourth order method, with a variable time step

$$dt = dt_{\min} + 10^{-3}(dt_{\max} - dt_{\min}) \left[\left(\frac{D}{r_p} \right)^3 - 1 \right]. \quad (6)$$

The parameters dt_{\max} and dt_{\min} (20 and 10 seconds respectively) were chosen such that the numerical integration error was ~ 100 times the floating point error, and that neighbouring values of K_{em} yielded significantly different spin pole data compared to floating point error. The data used to choose this dt was obtained using the reference asteroid configuration, described in appendix B.

2.2 Uncertainty model

To add noise to data generated via the above simulation, we use the following uncertainty model. Each asteroid spin vector Ω is assumed to be uncorrelated with other spin vectors, and we model uncertainty in the orientation and in the period as also uncorrelated. Consider a true spin vector Ω^* . For the sake of description, we work in coordinates in which $\Omega^* \parallel \hat{z}$. Then, expressing the observed spin vector Ω in spherical coordinates, we draw the polar angle from a normal distribution with standard deviation σ_θ centred on zero and the azimuthal angle from a uniform distribution. We also draw the ratio Ω/Ω^* from a log-normal distribution centred on one, with width σ_P/P , where $P = 2\pi\Omega$ is the period of the asteroid. Explicitly, the probability density function (PDF) of ρ is

$$P(\rho) = \frac{1}{\rho\sqrt{2\pi(\sigma_P/P)^2}} \exp\left(-\frac{\ln^2 \rho}{2(\sigma_P/P)^2}\right). \quad (7)$$

See figure 1 for an illustration of the uncertainty model. A log normal distribution is chosen such that $\rho > 0$, but since $\sigma_\rho \ll 1$ typically in our analysis, $P(\rho)$ is approximately Gaussian.

The log likelihood resulting from this uncertainty model is (excluding additive constants)

$$\ln \mathcal{L} = -\frac{1}{2} \sum_{i=0} \left[\frac{\cos^{-1}(\Omega_i^* \cdot \Omega_i / (\Omega_i^* \Omega_i))}{\sigma_\theta^2} + \frac{\ln(\Omega_i/\Omega_i^*)^2}{(\sigma_P/P)^2} + 2 \ln \frac{\Omega_i}{\Omega_i^*} \right]. \quad (8)$$

where Ω_i is the i th spin vector in the data set.

This model was chosen because it separates spin pole and period uncertainty. Therefore, if one is more precisely determined by measurement, σ_θ and σ_P/P can be adjusted separately in accordance.

2.3 Extracting density moments from spin data

Given synthetic data, an Affine Invariant MCMC Ensemble sampler was used to generate PPDs from flat priors. We use

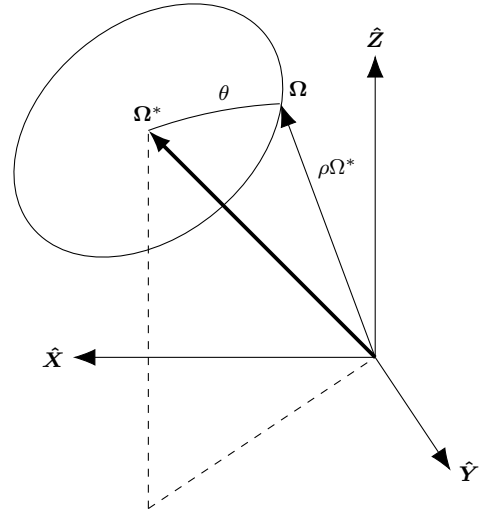


Figure 1. Diagram in the inertial frame of the uncertainty model used to define the probability that the true spin vector Ω^* should be observed as Ω . The parameter θ is drawn from a Gaussian with width σ_θ , and ρ is drawn from a log normal distribution with width σ_ρ .

the Python implementation `emcee` Foreman-Mackey et al. (2013). Our parameters were γ_0 , K_{20} , K_{22} , and K_{3m} (10 in total), and were bounded by $|\gamma_0| < \pi/4$, and bounds on K_{2m} given in equation A5. Note that γ_0 is degenerate with $\gamma_0 + \pi/2$ because both of these align the asteroid principal axes with the body-fixed axes. The other bounds were $|K_{3m}| < 1$. In general, spin data is most sensitive to γ_0 and K_{2m} , which we call the “first-order parameters.” We call K_{3m} the “second-order parameters.”

The MCMC was determined to converge when the fractional change in autocorrelation time (computed every 100 iterations) was one percent, and the number of iterations computed so far was more than 100 times the autocorrelation time. The MCMC fit also was set to terminate if more than 10^5 iterations were run, but this only occurred for fits in which the data quality was low, leading to degeneracies between the second order parameters (K_{3m}). This degeneracy could be removed by only fitting K_{2m} instead. About 10^4 iterations was often sufficient, which generally consumed about 7 hours of computation time on a super computer running 16 threads on 8 cores.

Before the MCMC was run, local minima in the likelihood were found via the Nelder-Mead algorithm implemented in `scipy` Gao & Han (2012). Generally, only one local minimum existed, except when $K_{22} = 0$ in which case rotational symmetry caused multiple values of γ_0 to be degenerate. Ensemble walkers were initialized near this local minimum, distributed by a Gaussian approximation of the likelihood, as determined via the Hessian of the likelihood at the minimum. Due to the high sensitivity of the angular velocity data to density moments, the minimization procedure sometimes failed to isolate the minimum likelihood. Therefore, a simpler simulation without the K_{3m} terms of equation 4 was first used to minimize likelihood as a function of the first-order parameters γ_0 and K_{2m} , and then the full simulation was used to find the second-order parameters K_{3m} with the first-order parameters fixed.

To further ensure convergence, we minimized with respect to data truncated after perigee at double the perigee distance. This cut-off was manually chosen. The minimum was then further refined by minimizing based on the full data, with the previous minimum as the initial estimate.

2.4 Density distribution constraints

The asteroid density distribution $\rho_A(\mathbf{r})$ is not uniquely constrained via tidal torque interactions because only the density moments $K_{\ell m}$ contribute to equation 4. For example, since the mass of the asteroid is unconstrained, $\rho_A(\mathbf{r})$ cannot be determined on an absolute scale. However, by making sufficient assumptions about the density distribution, we can nevertheless extract fluctuations in $\rho_A(\mathbf{r})$ across the asteroid from $K_{\ell m}$. To best understand the potential density distribution of an asteroid, an ensemble of models with differing assumptions is desired, so that common traits across the models can be identified. To this end, we thoroughly outline two possible models and discuss two more in appendix ??.

We assume that the asteroid's surface is known in the inertial frame from radar data. Since the asteroid tumbles during the encounter, we also assume that the center of mass of the asteroid is extracted. However, the density moments which are extracted from flyby data are known instead in the body-fixed frame.

We rotate the known surface of the asteroid to a new frame called the “hybrid frame” by translating such that the known center of mass is at the origin, then rotating such that Ω_0 points in the $+\hat{\mathbf{z}}_{\text{hybrid}}$ direction and $\hat{\mathbf{Y}}$ points in the $\hat{\mathbf{Y}}_{\text{hybrid}}$ direction. Since Ω_0 is exact, the surface in this hybrid frame is known exactly. The hybrid frame differs from the body-fixed frame only by a rotation around $\hat{\mathbf{z}}_{\text{hybrid}}$ of γ_0 . Such rotations affect density moments via

$$K_{\ell m}^{\text{hybrid}} = e^{-im\gamma_0} K_{\ell m}^{\text{body-fixed}}. \quad (9)$$

by equation A9. Thus, uncertainty on $K_{\ell m}^{\text{body-fixed}}$ (obtained from the encounter data) can be translated to uncertainty in $K_{\ell m}^{\text{hybrid}}$. Henceforth, we will operate only in the hybrid frame and suppress the label.

When the K_{3m} are extracted, 15 moments are known (excluding K_{00}). Since the asteroid mass cannot be determined by this analysis, it is convenient to additionally set the mass equal to its volume, so that the average density is one and thus the extracted densities can be interpreted as ratios of ρ/ρ_{avg} . Three more moments are redundant with the center of mass, such that only twelve finite elements are free. In cases where γ_0 is known very accurately such that the correction imposed by equation 9 is very small, it is numerically favourable not to impose this equation on K_{2m} . In this case, the three orientation constraints that set $K_{21} = \Im K_{22} = 0$ carry over to the hybrid frame so that there are nine degrees of freedom (DOF). Since γ_0 is precisely known for all cases studied in this paper, we will always study this case. We also place additional constraints that $0.25 < \rho < 3$ to ensure realistic densities.

To extract a density distribution, we use another MCMC given one of the two parametrizations of density distributions discussed below. The prior is set to be flat and nonzero for all configurations that obey the $0.25 < \rho < 3$ constraint. The likelihood used is set equal to the

Figure 2. Uncertainty in density, deviations from the true density, and maximum and mean significance of these deviations are plotted as a function of the observational precision of the flyby data. Five density distributions are computed for each value of observational precision (light dots) and their average is displayed (solid dots and lines). Each line represents a different choice in the number of free parameters used, with nine being maximal. Results show that few free parameters yield precise but inaccurate results, and that more yield imprecise but accurate results.

multivariate-Gaussian approximation of the posterior distribution for $K_{\ell m}$, extracted from flyby data. Otherwise, the MCMC parameters chosen were identical to those discussed in section 2.3.

2.4.1 Finite element model

Given values of $K_{\ell m}^{\text{body-fixed}}$ and their uncertainties extracted from encounter data, there are many ways to extract a density distribution. Here, we outline a method termed the “finite element” model. We divide the asteroid into N finite elements of uniform density and use the density ρ_i of each as parameters. The four constraints imposed by the known mass and center of mass of the asteroid (seven with K_{21} and $\Im K_{22}$ are also fixed) are used to constrain some of these ρ_i . The constrained densities are easily computed since the asteroid mass μ_A and the product $I_A K_{\ell m}$ are both linear functions of ρ_i . Because $K_{\ell m} = 0$ implies that $I_A K_{\ell m} = 0$, computing the constrained densities is simply a matrix inversion.

The size and location of the elements must be chosen before extracting their densities. Best results generally require elements of equal size to be chosen. To remove the dependence on this choice, density distributions for many distinct element layouts can be extracted and the density of each point in the asteroid can be randomly sampled from any of these solutions to yield estimates for the mean density and uncertainty in density at each point.

The value of N must be carefully chosen, since it embodies a balance between the precision and accuracy of the resulting distribution. If N is set equal to the number of data points, an accurate solution is guaranteed, but uncertainties are inflated. If N is chosen lower, the choice of element layout might exclude a distribution that exactly matches $K_{\ell m}$, but uncertainties are diminished due to less redundancy in the model. To select our value of N , we extract density distributions for moments extracted from simulated flyby data of the reference asteroid. We assume an ellipsoidal shape consistent with uniform asteroid density and extract 5 density distributions for it using this finite element model. We do this for multiple values of observational precision on the rotational period of the asteroid. Figure 11 displays the resulting average uncertainty on ρ_i for each of the five extractions (σ_ρ/ρ), as well as the average deviation from the truth ($\Delta\rho/\rho$), and displays the maximum and mean significance of these deviations ($\Delta\rho/\sigma_\rho$). The figure demonstrates that model accuracy is not a significant effect until the number of DOF is $\lesssim 3$, at which point $\Delta\rho/\sigma_\rho$ rises greatly. Uncertainty, however, is lower for 7 or 5 DOF than it is for 9. To balance accuracy and precision, we choose to use this lumpy

model with 5 DOF henceforth, meaning we choose $N = 12$ finite elements (using the $K_{21} = \Im K_{21} = 0$ constraint).

2.4.2 Lumpy model

A drawback of the finite element model is that the generated density distribution might not be representative of the asteroid if the elements are not optimally placed. We therefore describe an alternate model, which includes the positions of the elements as parameters at the cost of larger elements and therefore lower resolution. We call this model the “lumpy” model.

Suppose the asteroid is formed of N constant-density, possibly overlapping “lumps,” enclosed within a constant-density substrate whose surface is visible to observers. The lumps and the substrate are described by the mass added to the substrate by a lump μ_i , the position of its center of mass \mathbf{r}_i (relative to the asteroid’s center of mass), its density moments $K_{\ell m}^{(i)}$, and its length scale a_i . Here, i denotes the index of the lump where the substrate is $i = 0$. We do not need to include I_i as a free parameter because these lumps have constant density, so that $I_i = \mu_i a_i^2$. Furthermore, by requiring that a lump’s density moments be computed relative to the center of mass of the lump, we have $K_{1m} = 0$.

The translation rules of spherical harmonics give that the asteroid properties in the hybrid frame are

$$K_{\ell m} = \left[\sum_{i=0}^N \frac{a_i^2 + r_i^2}{a_A^2} \mu_i \right]^{-1} \times \left[\sum_{i=0}^N \sum_{\ell' m'} \mu_i \frac{a_i^{\ell'}}{a_A^\ell} R_{\ell - \ell', m - m'}(\mathbf{r}_i) K_{\ell' m'}^{(i)} \right] \quad (10)$$

where the sum limits are $0 \leq \ell' \leq l$ and $-\ell' \leq m' \leq \ell'$. We also have total mass and center of mass constraints:

$$\mu_A = \sum_{i=0}^N \mu_i, \quad 0 = \sum_{i=0}^N \mu_i \mathbf{r}_i. \quad (11)$$

Additional constraints can be imposed on $K_{\ell m}^{(i)}$ if desired. For example, we can require that the lumps be ellipsoids, so that $K_{3m}^{(i)} = 0$. Additional rotational symmetries also constrain K , with the most extreme case being that spherical lumps have $K_{\ell m} = 0$ for $\ell > 0$. However, $K_{00} = 1$ is guaranteed by definition, meaning that each spherical lump has only five DOF (a_i , μ_i , and \mathbf{r}_i). The substrate has one degree of freedom, since only μ_0 is unknown. Thus, this lumpy model has $5N - 3$ total DOF.

3 RESULTS

To demonstrate our interior-probing methodology, we provide a full density distribution retrieval applied to synthetic data for the asymmetric reference asteroid. We first introduce the retrieval capabilities regarding density moments, then we turn to the constraints that can be derived reliably on the density distribution. For both level of information retrieval, we find that the results are consistent with the properties used to generate the synthetic data.

3.1 Density moments

Figure 3 shows our synthetic spin data. The best-fitting model is overlaid in the top panel and residuals are shown in the bottom panel. Uncertainties are plotted on the residuals corresponding to the square root of the diagonal entries of the covariance matrix (correlations not included). The fit results are clearly consistent with the data.

Figure 4 shows a corner plot of the PPDs of the ten parameters (namely γ_0 and $K_{\ell m}$ for $\ell \leq 3$), marginalized to functions of one (histograms) or two (contours) variables. The true parameters are shown as lines. Note that the true parameters usually lie within 1 or 2σ of the $\Delta K_{\ell m} = 0$, where $\Delta K_{\ell m}$ is the difference between the posterior $K_{\ell m}$ and the true $K_{\ell m}$. The PPDs are generally Gaussian and sometimes show correlation between parameters, but no continuous degeneracy occurs. We performed 48 independent minimizations of the likelihood before the MCMC fit began, each with an initial point chosen randomly in the parameter space. All converged to the same minimum, demonstrating that the model lacks discrete degeneracy as well.

3.2 Density distribution

Density moments of the kind described above were extracted for the asymmetric and symmetric reference asteroids. The finite element model was then used to extract density distributions from these moments, and propagate uncertainties. Five DOF were used rather than the maximum possible number of nine, and 20 different finite element layouts were used to generate sample density distributions to avoid dependence on the manually-chosen layout. The resulting density distributions and uncertainties are displayed in figure 5.

The figure demonstrates that the finite element model successfully extracts a uniform density distribution. This property of the model was observed to be robust even for asteroids of different shapes. For the reference asteroid observational set-up, the uncertainty on observations is such that the density distribution is constrained to about **JTD: number**. The dependence of this constraint on the observational set-up is discussed in section 4.1.

The lumpy model, however, fails for a uniform asteroid. This is because the data is consistent with a massless lump placed anywhere in the asteroid, such that the model is underdetermined even when only one lump is attempted to be extracted. This failure of the lumpy model can be interpreted as evidence that the true density of the asteroid is close to uniform.

We also analyze asteroids of non-uniform density to assess the features our density-extraction models are most sensitive to. We employ an asteroid of the same shape as the asymmetric asteroid, and in the same flyby scenario. But we place a solid core of radius 500 m and density three times the surrounding density at the center of the asteroid, which changes the asteroid density moments. New density moments are extracted via the process described in section 2.3 and the finite-element and lumpy models are used to extract density distributions shown in figure 6.

Figure 6 demonstrates disagreement between the models caused by their different assumptions. The finite element model produces a density distribution with a more massive

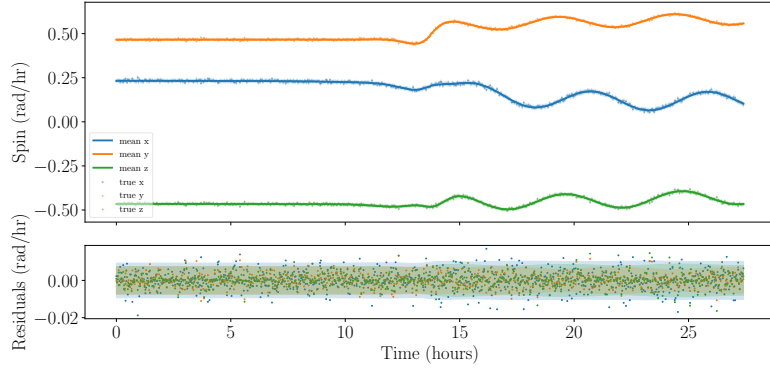


Figure 3. Data, best-fitting results, and residuals for a fit to synthetic data simulated for an asymmetric reference asteroid. Uncertainty bands are also shown. The best fit results appear consistent with the data.

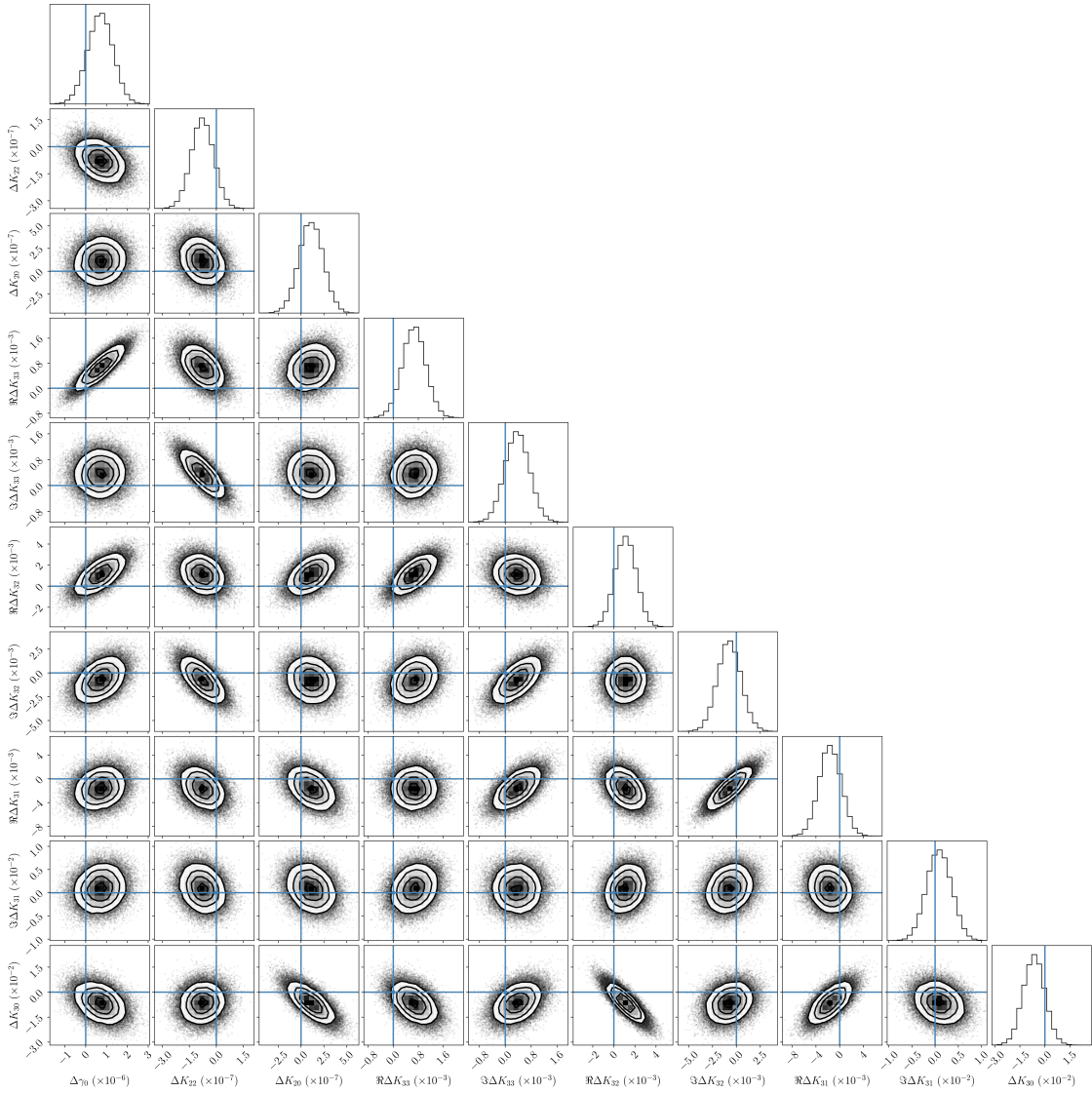


Figure 4. PPDs extracted from synthetic encounter data for the asymmetric reference asteroid. Samples from the MCMC fit are shown as individual points, and the contours enclose 1, 2, and 3 σ confidence regions. True values are shown as blue lines. PPDs are Gaussian and show no degeneracies.

Figure 5. Cross-sectional slices of the density distributions extracted via the finite element model for the asymmetric (*top*) and symmetric (*bottom*) reference asteroids. From left to right, the densities, deviations from the true density, uncertainties, and significance of the deviations are plotted.

Figure 6. Cross-sectional slices of the density distributions extracted via the finite-element (*top*) and lumpy (*bottom*) models for an asteroid with a centered core. From left to right, the densities, deviations from the true density, uncertainties, and significance of the deviations are plotted.

center, but the density of the core has been spread throughout the asteroid such that the density at the center is much less than three times the surrounding density. However, the lumpy model is designed to detect discrete changes in density distribution, and identifies the boundary of the core very accurately. The same density moments can be achieved via a smoothed density distribution, similar to the one produced by the finite element model. Therefore, neither model is more correct in the general case, but they can be used to explore different scenarios.

4 DISCUSSION

In this section, we discuss the sensitivity of our results to the properties of the asteroid encounter system. We start with the encounter properties that are required to adequately constrain the asteroid’s density moments and distribution, and further discuss the properties of Jupiter encounters compared to Earth encounters. Finally, we discuss in greater detail which features of an asteroid density distribution can be extracted by our models and which cannot be.

4.1 Dependence of uncertainty on encounter properties

Density density moment uncertainty is determined by the quality of the data set, but its physical relevance is not obvious. Uncertainty on the density distribution is much more physically motivated, but its value depends on the choice of model used. We therefore investigate the dependence of both uncertainties on encounter properties in this section.

For the density moments, we define their 1σ uncertainty as the range containing 68.27% of the PPD centred on the median. 2σ posterior uncertainty is defined likewise for 95.45% of the PPD. For the density distribution, we produce an uncertainty map which is the standard deviation of the densities produced by 1000 samples each from five different finite element extractions with different element layouts. We report the average uncertainty computed over this uncertainty map.

The encounter parameters we discuss are a mix of properties of the observational campaign (i.e., the cadence of observations, gaps in data, and uncertainty in the spin pole and period of the asteroid), and the physical properties of the asteroid (i.e., the true density moments, rotational period, perigee, excess velocity, initial spin pole direction, and length). As a rule-of-thumb, we say that a parameter becomes too large (or small) to allow for useful constraints on asteroid density when the uncertainty on the density σ_ρ becomes greater than some threshold value. We use both

Encounter property	$\sigma_\rho/\rho = 100\%$	20%
Perigee (r_p , Earth radii)	<7.9	<4.7
Spin pole uncertainty (σ_θ , °)	<2.8	<0.5
Spin period uncertainty ($P_\omega \sigma_\rho$, ms)	<15	<3.1
Asteroid length (a_A , m)	>180	>1100
Cadence (Δt , min)	<38	<2
Data gap (T_{gap} , hr)	<1.8	<0
Period (P_ω , hr)	>4.3	>9.5

Table 1. For each encounter property discussed in section 4, the properties that lead to density uncertainty equal to 100% (20%) of the local density are shown in the middle (right) columns. The reference asymmetric asteroid is used. The 20% threshold is very restrictive, but the 100% threshold is more achievable and demonstrates the thresholds in the right column are not hard cut-offs.

threshold values of $\sigma_\rho/\rho = 20\%$ and 100% , and the resulting limits on the various encounter properties are displayed in table 1.

JTD: Discuss conclusions .

Uncertainties on the density moments, which do not depend on models used, are displayed as a function of encounter properties in figures 9 and 10. The properties corresponding to the 20% and 100% density uncertainty thresholds are indicated with red lines, and a dotted black line indicates the properties of the reference asteroid. The initial spin pole direction and the asteroid shape are also shown in figures 8 and 7 respectively.

JTD: Discuss conclusions .

Additional data and analysis and description for this relationship between encounter parameters and uncertainties are given in appendix E

4.2 Comparison of Jupiter and Earth encounters

If sufficiently accurate spin pole data can be detected for non-Earth encounters, it may be possible to extract density moments for encounters with larger planets. In this section, we run our reference asteroid through a Jupiter encounter to analyze the differences in uncertainty.

The physical parameters of the asteroid body are kept the same as the Earth encounter case (listed in appendix B), as are the observational uncertainty and cadence. The orbit is adjusted for the Jupiter case by setting a perijove distance of $r_p = 5$ Jupiter radii (compared to perigee radius $r_p = 5$ Earth radii for the Earth encounter). The excess velocity does not strongly affect $\sigma(K_{\ell m})$ as shown in section E1, so we keep it at the reference value. The ratio between the posterior uncertainties in the Jupiter and the Earth encounters are shown in table 2. In all cases, the Jupiter posteriors are more uncertain than Earth posteriors.

These uncertainty ratios can be understood as follows.

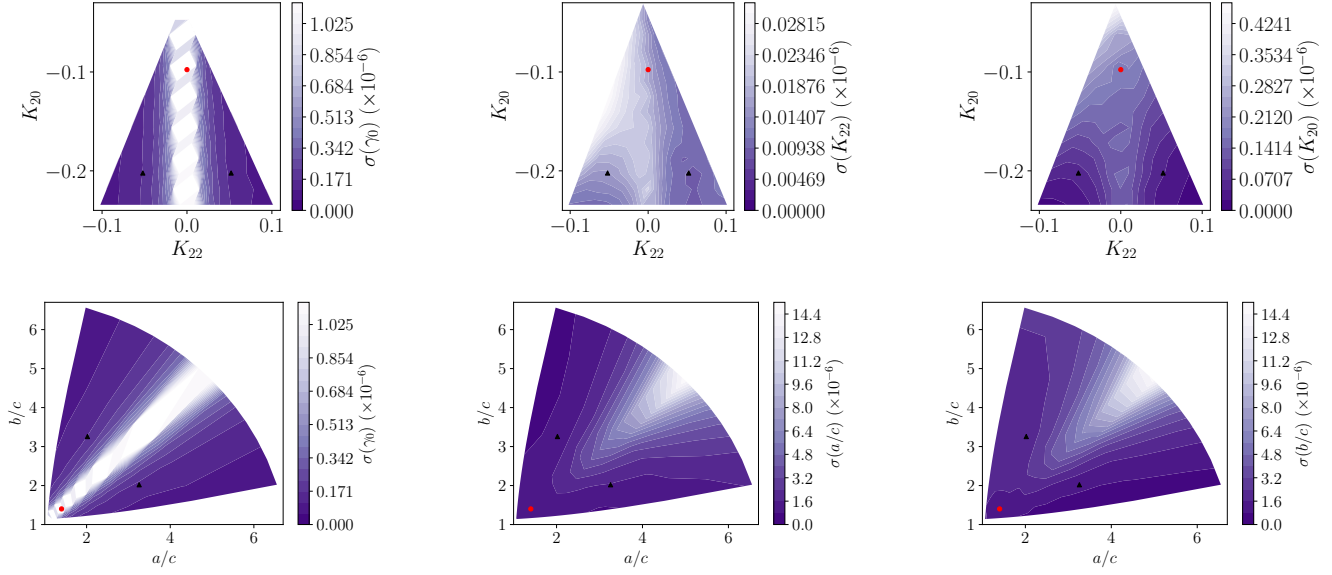


Figure 7. 1σ posterior uncertainty for first-order parameters γ_0 , K_{22} , and K_{20} (top row) and γ_0 , a/c , and b/c (bottom row). Also shown as black points are the reference asteroid shapes: symmetric (red circle) and asymmetric (black triangle). Symmetric asteroids ($K_{22} = 0$ or $a/c = b/c$) show increased posterior uncertainty, but otherwise posterior uncertainty is roughly constant.

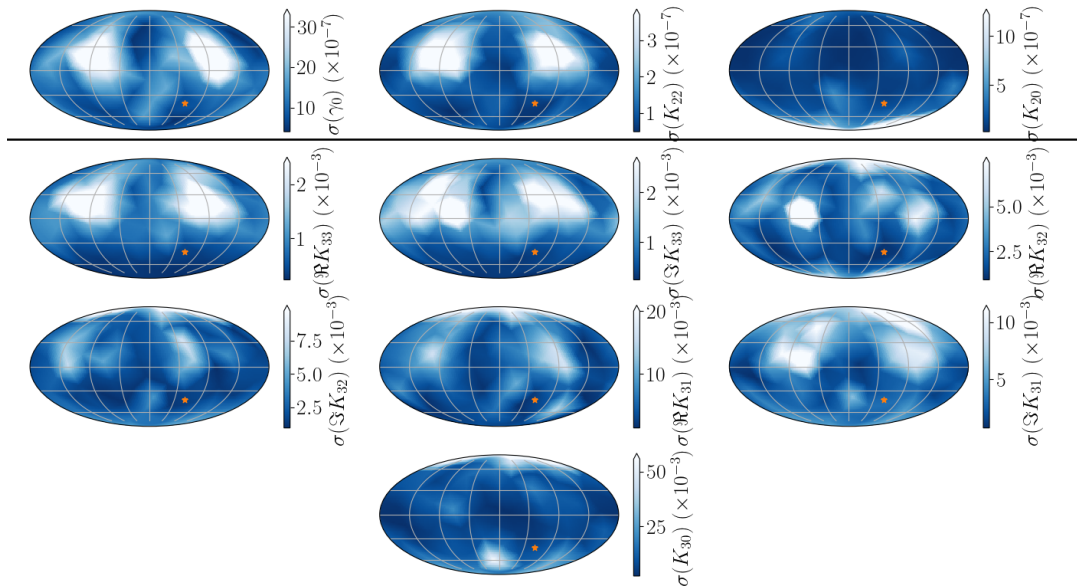


Figure 8. 1σ uncertainties for the first-order parameters (top) and second-order (bottom) as a function of the initial direction of spin in the inertial frame. All maps are made in the Mollweide projection. The orange star indicates the reference spin pole. The red contours enclose regions the 20% (dotted) and 100% (solid) σ_ρ/ρ cut-off. Posterior uncertainty depends similarly on initial spin pole direction for all parameters

$K_{\ell m}$	$\sigma(K_{\ell m})_{\text{Jupiter}}/\sigma(K_{\ell m})_{\text{Earth}}$
γ_0	1.6
K_{22}	2.3
K_{20}	11
$\Re K_{33}$	18
$\Im K_{33}$	18
$\Re K_{32}$	18
$\Im K_{32}$	18
$\Re K_{31}$	25
$\Im K_{31}$	10
K_{30}	53

Table 2. Ratio of posterior uncertainty for all density moments $K_{\ell m}$ between an Earth encounter and a Jupiter encounter with identical properties except for an increased perigee. Observational uncertainty and cadence are assumed to be equivalent for the Jupiter and Earth encounters. Without taking the frequencies of close encounters into account, massive planets such as Jupiter yield less precise density moment estimates.

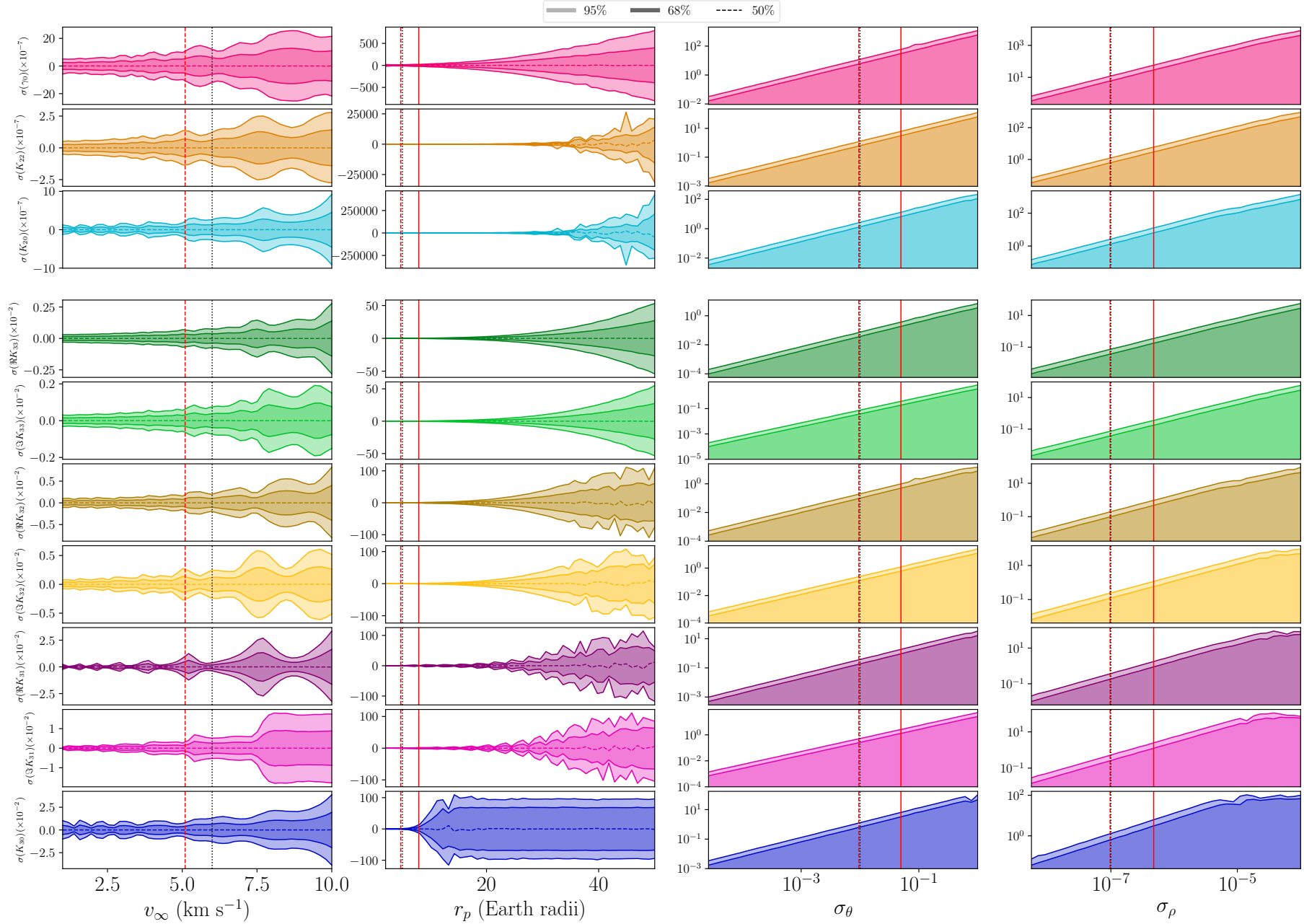


Figure 9. 1 and 2σ confidence intervals for the first-order parameter PPDs (*top*) and second-order parameters (*bottom*) as a function of (left to right) perigee, excess velocity, spin pole uncertainty, and period uncertainty. The vertical dashed line indicates the reference asteroid values. The red vertical lines indicate when $\sigma(K_{3m}) = 0.01$.

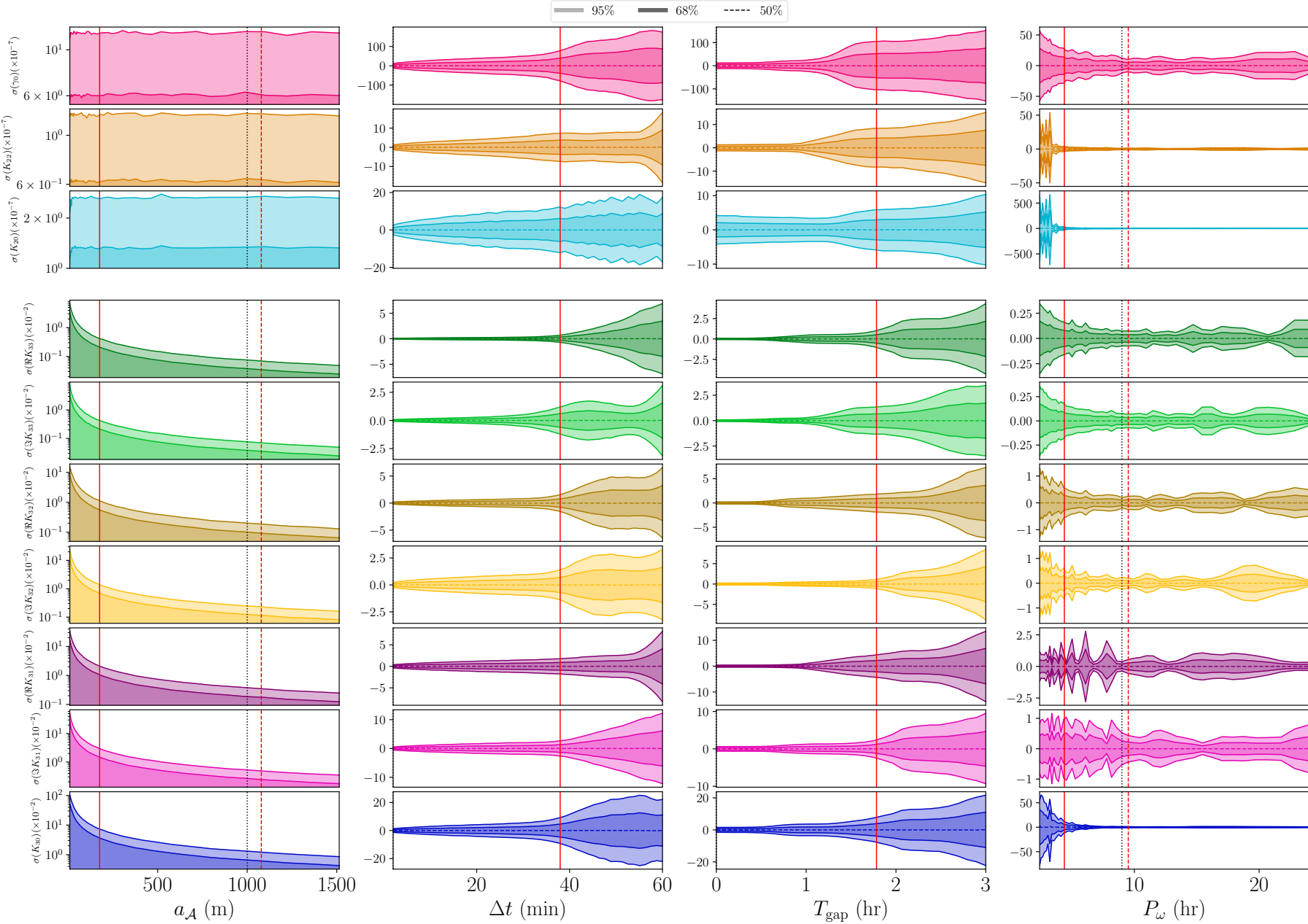


Figure 10. 1 and 2σ confidence intervals for the first-order parameter PPDs (*top*) and second-order parameters (*bottom*) as a function of (left to right) asteroid length, observational cadence, data gap at perigee, and rotational period. The vertical dashed line indicates the reference asteroid values. The red vertical lines indicate when $\sigma(K_{3m}) = 0.01$.

be slightly worse than in the case of Earth, which is seen in table 2.

The second-order terms are damped by an additional factor of a_A/D , which decreases if a massive central body is used. Since Jupiter is about 10 times larger in radius than Earth, we expect that the K_{3m} terms are about ten times more uncertain than the K_{2m} components, which is the case.

The $K_{\ell 0}$ components differ in that the posterior uncertainty increase for a Jupiter encounter over an Earth encounter is about five times greater for $K_{\ell 0}$ than other moments of the same ℓ . In fact, K_{30} essentially fills the prior. In section E6, we noted that $K_{\ell 0}$ is particularly uncertain when the asteroid does not tumble after the perigee. In this case, the Jupiter encounter resulted in less tumbling than the Earth encounter, so the larger increase in uncertainty in $K_{\ell 0}$ shown in table 2 is expected.

There are additional effects of central body mass which are not captured in this analysis. For example, encounters with massive planets are more plentiful, so that observation for a fixed period of time will lead to a larger number of observed encounters conducive to low-uncertainty moment extraction (large a_A , small r_p , etc.). The distribution of r_p in this encounter sample will also change; the ratio of the orbit impact parameter (the distance between the orbit asymptotes and the central body) to perijove distance is

$$\frac{b}{r_p} = \sqrt{1 + 2 \frac{G\mu_B}{r_p v_\infty^2}}. \quad (12)$$

It was mentioned above that the observable perigee distance r_p increases with $a_B \sim \mu_B^{1/3}$, so that $\frac{b}{r_p}$ is larger for more massive planets and therefore the same impact parameter leads to lower perijove. Other effects, such as a change in the physical properties of the encountering asteroids or decreased observational uncertainty due to the distance between Jupiter and Earth-based telescopes, may also affect the fit uncertainties. Which of these contradicting effects dominates is not immediately clear, and depends on the asteroid population near Jupiter and the observation method.

4.3 Finite element model DOF

The number of elements N used for the finite element model can be freely chosen. As discussed in section ??, seven of these are fixed by various constraints on the asteroid density distribution. There are 16 density moments with $\ell \leq 3$, so $N = 16$ with nine DOF is the largest number of parameters the model can support. However, maximizing the DOF adds model-induced uncertainty to our results. This uncertainty can be reduced by reducing N , but with $N < 16$, a solution perfectly matching the extracted moments is not guaranteed. There is therefore a trade-off between the average density uncertainty σ_ρ and the accuracy, which can be represented as the deviation of the density distribution from the true distribution $\Delta\rho$.

We investigate this trade-off by extracting five density distributions with five different finite-element layouts from moments extracted from synthetic data of the asymmetric reference asteroid. For each point in the asteroid, 1000 samples are drawn from each of the five density distributions. We use the standard deviation of the 5000 samples as the uncertainty at that point, and the mean of the samples as

Figure 11. The average uncertainty σ_ρ and deviation from the truth $\Delta\rho$ of density distributions extracted by the finite element model with varying degrees of freedom. 5 DOF appears to optimize the trade-off between the model-induced uncertainty caused by too many DOF and the inaccuracy caused by too few.

the density. We then compute σ_ρ and $\Delta\rho$ by averaging over every point in the asteroid. We do this for 9 (maximal), 7, 5, 3, and 2 DOF. Additionally, we vary the precision σ_P of the data set used to extract the density moments, and plot σ_ρ and $\Delta\rho$ as a function of σ_P . The result is shown in figure 11

The figure demonstrates the expected behaviour that the uncertainty of the result increases with additional degrees of freedom, and its accuracy decreases. **JTD: Comment**. For these reasons, we use 5 DOF which corresponds to $N = 12$ throughout this paper.

Figure 11 also demonstrates that σ_ρ reaches a plateau for large σ_P . For data this uncertain, the prior constraints that the density of the asteroid take on physically meaningful values are more constraining than the actual data, leading to less dependence on the data quality. **JTD: Further comment**.

4.4 Comparisons between density distribution models

In section 3.2, we displayed density distributions extracted via the lumpy model with $N = 1$ lumps. When $N = 1$, the model has two DOF, meaning that the density distribution can be determined only via the fit results for K_{2m} , rather than the relatively poorly constrained K_{3m} . Therefore, we also explore a density distribution with $N = 2$ lumps, which has seven DOF.

JTD: Continue

JTD: Possibly discuss moved core

5 CONCLUSIONS

We derived a novel, arbitrary-order equation for the tidal torque experienced by an asteroid during an encounter with a planet of arbitrary shape and mass distribution. The tidal torque equation (equation 4) revealed that the angular velocity of the asteroid over time depends strongly on $K_{\ell m}$ and the initial orientation. We then built a fast simulation for an asteroid encounter, truncating the equation at second-order, and used the simulation to extract first- and second-order density moments from synthetic spin pole data via a Markov Chain Monte Carlo fit. We observe the following general properties of the moments:

(i) The second-order moments K_{3m} are roughly a factor of $\frac{a_A}{r_p}$ more uncertain than the first-order moments, where a_A is proportional to the asteroid radius and r_p is the perigee distance. For our reference asteroid, this fraction was about 10^{-5} .

(ii) The second-order moments that measure small-scale variations in density (i.e., $|m|$ is large) are generally less uncertain. It is often possible to measure $K_{3|m|}$ for large m even when K_{30} is not resolved.

- (iii) Extracted density moments are generally more precise when the asteroid leaves the encounter tumbling.
- (iv) The oblateness of the central body cannot be ignored without generating incorrect density moment estimates.

We assessed the posterior uncertainty generated by the fit process by adjusting various properties of an asteroid on an Earth encounter. The precise thresholds we measure (table 1) show that the observational uncertainty and perigee of the asteroid orbit are the most difficult requirements to meet, with perigee $\lesssim 6$ Earth radii, spin pole uncertainty $\lesssim 1^\circ$, and period uncertainty $\lesssim 10$ ms. However, these thresholds depend on the model used to extract a density distribution, and useful information may be able to be extracted when they are not achieved by using a different model.

Finally, we presented three fast, linear methods for extracting density distributions (together with uncertainties) from the density moments and the shape of the asteroid. The extracted density distributions are largely consistent with the true distributions in all cases we tested. Slight adjustments to K_{3m} dramatically change the overall distribution, so that they are not very precise. Indeed, the models sometimes predict negative density (though more complicated models could be made not to). Errors in the shape estimate of the asteroid also distort the density distribution, but the resulting distributions provide hints as to exactly where the shape is incorrect. Large-scale properties of the asteroid's true distribution, such as whether the mass is located in the middle or on the edges, are often observable. Two of the models presented (the harmonic and lumpy models) are flexible in their number of parameters, so that if only these large-scale properties are necessary, a small set of parameters can be chosen to prevent over-fitting.”

ACKNOWLEDGEMENTS

We warmly thank Emmanuel Jehin, Maxime Devogele, and Marin Ferrais for meeting with the authors to discuss this work and pointing out possible future initiatives. JTD also thanks the MIT UROP office for funding his work. This paper made substantial use of MIT Supercloud's facilities.

DATA AVAILABILITY

The asteroid simulation, fit process, and density moment extraction code are available on [GitHub](#).

REFERENCES

- Ashenberg J., 2007, *Celestial Mechanics and Dynamical Astronomy*, 99, 149
- Benson C. J., Scheeres D. J., Moskovitz N. A., 2020, *Icarus*, 340, 113518
- Berthier J., et al., 2020, *Icarus*, 352, 113990
- Boué G., Laskar J., 2009, *Icarus*, 201, 750
- Brown T., et al., 2013, *Publications of the Astronomical Society of the Pacific*, 125, 1031
- Carroll K., Faber D., 2018, in *Proceedings of the 69th International Astronautical Congress*.
- Descamps P., et al., 2020, *Icarus*, 345, 113726
- Devogèle M., et al., 2021, *Monthly Notices of the Royal Astronomical Society*, 505, 245
- Foreman-Mackey D., Hogg D. W., Lang D., Goodman J., 2013, *Publications of the Astronomical Society of the Pacific*, 125, 306
- Gao F., Han L., 2012, *Computational Optimization and Applications*, 51, 259
- Giorgini J., Benner L., Nolan M., Ostro S., 2005, in *AAS/Division of Dynamical Astronomy Meeting# 36*. pp 02–01
- Giorgini J. D., Benner L. A., Ostro S. J., Nolan M. C., Busch M. W., 2008, *Icarus*, 193, 1
- Hirabayashi M., Kim Y., Brozović M., 2021, *Icarus*, 365, 114493
- Hou X., Scheeres D. J., Xin X., Mar 2017, *Celestial Mechanics and Dynamical Astronomy*, 127, 369
- Kaasalainen M., 2001, *Astronomy & Astrophysics*, 376, 302
- Kaiser N., et al., 2002, in *Survey and Other Telescope Technologies and Discoveries*. pp 154–164
- Larson S., Brownlee J., Hergenrother C., Spahr T., 1998, in *Bulletin of the American Astronomical Society*. p. 1037
- Lee H.-J., et al., 2022.
- Makarov V. V., Goldin A., Tkachenko A. V., Veras D., Noyelles B., 2022.
- Moskovitz N. A., et al., 2020, *Icarus*, 340, 113519
- Naidu S. P., Margot J.-L., 2015, *The Astronomical Journal*, 149, 80
- Pater D. I., Lissauer J. J., 2015, *Planetary sciences*, 2 edn. Cambridge University Press
- Paul M. K., 1988, *Celestial mechanics*, 44, 49
- Pravec P., et al., 2014, *Icarus*, 233, 48
- Richardson D. C., Bottke W. F., Love S. G., 1998, *Icarus*, 134, 47
- Richardson J. E., Melosh H. J., Greenberg R. J., O'Brien D. P., 2005, *Icarus*, 179, 325
- Scheeres D., Ostro S., Werner R., Asphaug E., Hudson R., 2000, *Icarus*, 147, 106
- Scheeres D. J., Marzari F., Rossi A., 2004, *Icarus*, 170, 312
- Smalley K., Garradd G., Benner L., Nolan M., Giorgini J., Chesley S., Ostro S., Scheeres D., 2005, *International Astronomical Union Circular*, 8477, 1
- Souchay J., Souami D., Lhotka C., Puente V., Folgueira M., 2014, *Astronomy & Astrophysics*, 563, A24
- Souchay J., Lhotka C., Heron G., Hervé Y., Puente V., Lopez M. F., 2018, *Astronomy & Astrophysics*, 617, A74
- Stokes G. H., Evans J. B., Viggh H. E., Shelly F. C., Pearce E. C., 2000, *Icarus*, 148, 21
- Tyson J. A., 2002, *Survey and Other Telescope Technologies and Discoveries*, 4836, 10
- Valvano G., Winter O. C., Sfair R., Machado Oliveira R., Borderes-Motta G., Moura T., 2022, *Monthly Notices of the Royal Astronomical Society*, 510, 95
- Wright E. L., et al., 2010, *The Astronomical Journal*, 140, 1868
- Yu Y., Richardson D. C., Michel P., Schwartz S. R., Ballouz R.-L., 2014, *Icarus*, 242, 82
- van Gelderen M., 1998, in *The shift operators and translations of spherical harmonics*.

APPENDIX A: TIDAL TORQUE & EQUATIONS OF MOTION

In this appendix, we derive the equations of motion used to simulate the asteroid angular velocity during the encounter. In particular, we describe our coordinates (section A1) for an encountering asteroid's position and orientation, and we parametrize its density distribution via its “density moments” (section A2). Then we derive an arbitrary-order

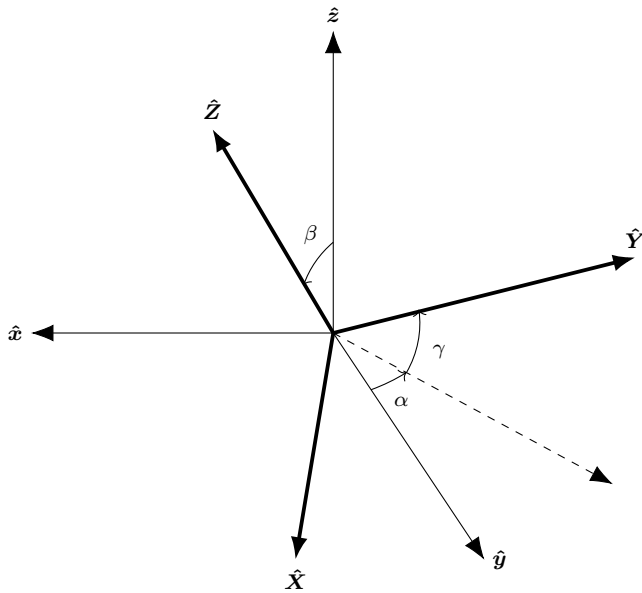


Figure A1. $z - y - z$ Euler angles used in this work to express the orientation of the asteroid. Orientation is expressed as a rotation from the body-fixed axes (lowercase) to the inertial axes (bold and uppercase). The origins are co-located for demonstration purposes.

equation for tidal torque (section A3) and write the equations of motion for the system (section A4). We do not consider any third-body perturbations, and we assume that the body being encountered (the central body, e.g. a planet) is much more massive than the asteroid.

A1 Coordinates

We make use of two frames of reference to model this system. One is the “inertial frame,” with axes denoted by \hat{X} , \hat{Y} , \hat{Z} and origin placed at the central body’s centre of mass. \hat{X} points from the central body to the asteroid periapse, and \hat{Z} points parallel to the orbit angular momentum. We assume that the mass distribution of the central body is known in this inertial frame.

Our second frame is the “body-fixed” frame, denoted by \hat{x} , \hat{y} , \hat{z} . Each axis in this frame is aligned with a principal axis and rotates with the asteroid, with its origin at the asteroid’s centre of mass. For definiteness, we define \hat{z} to be the principal axis with maximal moment of inertia (this is the short axis mode, to use the vocabulary of Ref. Kaasalainen (2001)). In general, we use capital letters to denote vectors in the inertial frame and lowercase vectors to denote vectors in the body-fixed frame.

The difference between the origins of the body-fixed and inertial frames is the position of the asteroid. We represent the relative orientations by $z - y - z$ Euler angles α , β , and γ , such that a matrix M rotating from the body-fixed to the inertial frame ($M\mathbf{r} = \mathbf{R}$) is given by

$$M = R_z(\alpha)R_y(\beta)R_z(\gamma). \quad (\text{A1})$$

Here, $R_i(\theta)$ is a rotation around the unit vector i by θ (figure A1).

A2 Density moments

In the next section, it will be shown that only certain parameters of the asteroid density distribution affect tidal torque called “density moments.” First, we define the unnormalized spherical harmonics $Y_{\ell m}(\theta, \phi) = P_{\ell m}(\cos \theta)e^{im\phi}$, where $P_{\ell m}$ are the associated Legendre Polynomials without the Condon-Shortley phase. The regular and irregular spherical harmonics then defined as

$$\begin{aligned} S_{\ell m}(\mathbf{r}) &= (-1)^m (\ell - m)! \frac{Y_{\ell m}(\hat{\mathbf{r}})}{r^{\ell+1}} \\ R_{\ell m}(\mathbf{r}) &= (-1)^m \frac{r^\ell}{(\ell + m)!} Y_{\ell m}(\hat{\mathbf{r}}). \end{aligned} \quad (\text{A2})$$

These spherical harmonics obey many useful identities summarized in Ref. van Gelderen (1998), which are also useful for quantum mechanics.

We define the density moments of an asteroid in equation 1. Note that these are complex. The length defined in equation ?? can be thought of as akin to the radius of the asteroid (a spherical, uniform-density asteroid has radius $a_A \sqrt{5/3}$). Both equations ?? and 1 should be computed in the body-fixed frame.

Equations ?? and 1 can be extended to the central body:

$$\begin{aligned} J_{\ell m} &= \frac{1}{\mu_B a_B^\ell} \int_B d^3 r \rho_B(\mathbf{r}) R_{\ell m}(\mathbf{r}) \\ a_B^2 &= \frac{1}{\mu_B} \int_B d^3 r \rho_B(\mathbf{r}) r^2. \end{aligned} \quad (\text{A3})$$

which should be computed in the inertial frame.

Note that both $J_{\ell m}$ and $K_{\ell m}$ are unitless. We call them “moments” because the $R_{\ell m}(\mathbf{r})$ contains an r^ℓ dependence so that $K_{\ell m}$ is the ℓ th density moment of the asteroid. The gravitational potential field of the asteroid can be written entirely in terms of $K_{\ell m}$ and a_A , so we expect not to need any information about the density distribution of the asteroid beyond these parameters to compute tidal torque.

These moments share several key properties which we discuss before continuing. Firstly, for real mass density, properties of the spherical harmonics imply that $K_{\ell m} = (-1)^m K_{\ell, -m}^*$. Therefore, the set of $K_{\ell m}$ for $\ell < \ell_{\max}$ contains ℓ_{\max}^2 degrees of freedom. However, some of these degrees of freedom are redundant with the choice of coordinates as we discuss next.

By definition, $K_{00} = 1$. Furthermore, $K_{1m} = 0$ since the body-fixed frame is centred on the asteroid centre of mass. Further calculation reveals that the alignment of the body-fixed frame with the asteroid principal axes also forces $K_{21} = 0$ and $\Im K_{22} = 0$ and the same for $m < 0$. The only physical density moments for $\ell \leq 2$ are therefore K_{22} and K_{20} , which are related to the moment of inertia around each principal axis by equation 5. Incidentally, the definition of a_A was chosen to satisfy equation 5.

The physical meaning of K_{22} and K_{20} can also be interpreted via a special case: if the asteroid is a uniform-density triaxial ellipsoid, the moments of inertia are simple to compute in terms of the semi-axis lengths and can be compared to those found in equation 5. This yields semi-axis lengths

ℓ	$\Re K_{\ell 3}$	$\Im K_{\ell 3}$	$\Re K_{\ell 2}$	$\Im K_{\ell 2}$	$\Re K_{\ell 1}$	$\Im K_{\ell 1}$	$K_{\ell 0}$
0							-
1					x	y	z
2			-	x,y	y,z	x,z	-
3	x,z	y,z	z	x,y,z	x	y	z

Table A1. Axes of mirror symmetry that imply zeroed density moments. For example, for mirror symmetries along \hat{y} or \hat{z} , $\Im K_{32} = 0$. Mirror symmetry along \hat{x} means $\rho_A(x, y, z) = \rho_A(-x, y, z)$. Dashes indicate that none of the mirror symmetries zero the moment in question. Since $r^2 > 0$ for $r \neq 0$, no symmetries set $a_A = 0$ either.

of

$$\begin{aligned} a &= \sqrt{\frac{5}{3}} a_A \sqrt{1 - 2K_{20} + 12K_{22}} \\ b &= \sqrt{\frac{5}{3}} a_A \sqrt{1 - 2K_{20} - 12K_{22}} \\ c &= \sqrt{\frac{5}{3}} a_A \sqrt{1 + 4K_{20}}. \end{aligned} \quad (\text{A4})$$

The physical meaning of the higher-order moments K_{3m} can be aided by assessing their symmetry properties. An asteroid that is mirror-symmetric along the \hat{x} axis (meaning $\rho_A(x, y, z) = \rho_A(-x, y, z)$) necessarily sets certain density moments to zero. Which density moments are zeroed by which mirror symmetries is outlined in table A1. Note that, while no mirror symmetries set K_{00} , K_{20} , or K_{22} equal to zero, mirror symmetries exist which zero all the other moments, including K_{3m} . $\Re K_{32}$, K_{31} , and K_{30} are the only K_{3m} components zeroed by only one axis. This will not affect our fit results for K_{3m} , but when we compute density moments for sample distributions, we find that most $K_{3m} = 0$.

Finally, the requirement that $\rho_A(\mathbf{r}) \geq 0$ everywhere restricts $K_{\ell m}$. In the case of K_{2m} , this fact and the constraint that I_z is larger than I_x or I_y requires K_{20} and K_{22} to fall in the triangle

$$-\frac{1}{4} \leq K_{20} \leq 0, \quad |K_{22}| \leq -\frac{K_{20}}{2}. \quad (\text{A5})$$

In practice, we also observe that $|K_{3m}| < 1$; often, $|K_{3m}| < 0.01$ even.

A3 Tidal torque

Derivations for the tidal torque experienced by a rigid body in the gravitational field of a larger mass have been computed by several previous studies Paul (1988); Hou et al. (2017); Boué & Laskar (2009); Ashenberg (2007), often in terms of the moment of inertia of the rigid body (or higher order moments of inertia), and to varying degrees of precision. A simple, first-order derivation is also easily computable in terms of the asteroid moment of inertia in the inertial frame.

Here, we present a novel derivation of the tidal torque to arbitrary orders in terms of the density moments of an asteroid defined in section A2. These density moments can be pre-computed and do not have to be re-evaluated every time-step.

Throughout this paper, we assume that the asteroid remains rigid throughout the encounter. We also assume no third-body perturbations from other Solar System objects.

(Actually, third-body perturbing objects are allowed if they are closer to the central body's centre of mass than the asteroid perigee distance. Then, their density moments can be included in the density moments of the central body and this derivation can still be used.) For the sake of simplicity, we also assume that the density moments of the central body are known and do not evolve with time (i.e., the central body's rotation is marginal compared to the timescale of the encounter).

The gravitational potential energy of the central body is, in its most general form,

$$V(\mathbf{R}') = -G \int_{\mathcal{B}} d^3 R \rho_B(\mathbf{R}) \frac{1}{|\mathbf{R} - \mathbf{R}'|}. \quad (\text{A6})$$

where ρ_B is the density distribution of the central body and \mathcal{B} indicates the central body's volume. All vectors here are written in the inertial frame. Given $|\mathbf{R}| < |\mathbf{R}'|$, Ref. van Gelderen (1998) gives the identity

$$\frac{1}{|\mathbf{R} - \mathbf{R}'|} = \sum_{\ell, m} R_{\ell m}(\mathbf{R}) S_{\ell m}^*(\mathbf{R}'), \quad (\text{A7})$$

where the sum is shorthand for $\sum_{\ell, m} = \sum_{\ell=0}^{\infty} \sum_{m=-\ell}^{\ell}$. We are interested in translating the potential energy of equation A6 to the body-fixed frame. To do this, we let $\mathbf{R}' = \mathbf{D} + \mathbf{U}$, where \mathbf{D} is the location of the asteroid in the inertial frame. We further define $\mathbf{U} = M\mathbf{u}$, where \mathbf{u} is in the body-fixed frame and M is the rotation matrix given by the Euler angles α , β , and γ (see section A1). The translation from \mathbf{R}' to \mathbf{U} is then attained by the identity

$$S_{\ell m}(\mathbf{R}') = \sum_{\ell', m'} (-1)^{\ell'} R_{\ell' m'}^*(\mathbf{U}) S_{\ell + \ell', m + m'}(\mathbf{D}), \quad (\text{A8})$$

provided by Ref. van Gelderen (1998), and from \mathbf{U} to \mathbf{u} is given by

$$\begin{aligned} Y_{\ell m}(M\mathbf{u}) &= \sum_{m'=-\ell}^{\ell} (-1)^{m+m'} \sqrt{\frac{(\ell - m')!(\ell + m)!}{(\ell + m')!(\ell - m)!}} \\ &\quad \times \mathcal{D}_{mm'}^{\ell}(M)^* Y_{\ell m'}(\mathbf{u}). \end{aligned} \quad (\text{A9})$$

Here, $\mathcal{D}_{mm'}^{\ell}(M)$ are the Wigner-D matrices, which are determined by the Euler angles α , β , and γ of M .

Equations A6 to A9 then provide formula for $V(\mathbf{u})$ expressed as a sum of integrals over \mathcal{B} of the central body density $\rho_B(\mathbf{R})$ times $R_{\ell m}(\mathbf{R})$. These are expressed via equation A3 as $J_{\ell m}$.

The tidal torque experienced by the asteroid (in the body-fixed frame) is given by

$$\boldsymbol{\tau}(\mathbf{u}) = \int_{\mathcal{A}} d^3 u \rho_A(\mathbf{u}) (\mathbf{u} \times (-\nabla_{\mathbf{u}} V(\mathbf{u}))) \quad (\text{A10})$$

where ρ_A is the density distribution of the asteroid and \mathcal{A} indicates the volume of the asteroid. Making use of one more identity concerning the derivatives of spherical harmonics:

$$\begin{aligned} \mathbf{u} \times \nabla R_{\ell m}(\mathbf{u}) &= \frac{1}{2} \left[(i\hat{x} - \hat{y})(\ell - m + 1) R_{\ell, m-1}(\mathbf{u}) \right. \\ &\quad + (i\hat{x} + \hat{y})(\ell + m + 1) R_{\ell, m+1}(\mathbf{u}) \\ &\quad \left. + 2im\hat{z} R_{\ell m}(\mathbf{u}) \right], \end{aligned} \quad (\text{A11})$$

tidal torque can now be expressed as a function only of $J_{\ell m}$, $K_{\ell m}$, a_A , a_B , and the asteroid orientation and position. This equation is given explicitly as equation 4. Some $K_{\ell m}$ terms

are written in this equation with $|m| > \ell$; these should all be taken to be zero.

Equation 4 possesses a few explicit properties which we discuss before writing the asteroid equations of motion. Firstly, K_{00} does not appear, so that τ is independent of asteroid mass. The mean density of the asteroid is therefore not constrained by tidal torque analysis. Secondly, torque is largest when D is small (as expected), with the leading order of τ proportional to D^{-3} . Thirdly, each $J_{\ell m} K_{\ell' m'}$ term is multiplied by $(a_B/D)^\ell (a_A/D)^{\ell'}$, the latter of which especially is small in most cases. Equation 4 can therefore be computed approximately by removing terms of large ℓ and ℓ' . For our analysis, we removed $\ell' > 3$ and we usually keep only $\ell = 0$. Note that $\ell = 1$ contributes nothing since $J_{1m} = 0$.

Further insight can be gained by remarking the value of the first-order of τ for particular Euler angle cases. Setting $\beta = 0$ produces diagonal Wigner- D matrices, and hence $\tau \parallel \hat{z}$ to first-order. Also, the component τ_z oscillates, so that for certain values of α and γ , $\tau = 0$. This $\beta = 0$ condition is equivalent to $\hat{z} \parallel \hat{Z}$ (see figure A1).

For $\beta = \pi/2$, there are two interesting cases. One is for $\alpha = \phi$ (or $\alpha = \pi + \phi$), where ϕ is the angle between the asteroid and the perigee. In this case, $\tau = 0$ to first-order. The second case is $\alpha = \phi \pm \pi/2$, when again $\tau \parallel \hat{z}$ and τ_z oscillates. At perigee ($\phi = 0$), these conditions are equivalent to $\hat{z} \parallel \hat{X}$ and $\hat{z} \parallel \hat{Y}$ respectively.

The $\tau \parallel \hat{z}$ cases are interesting because they do not induce tumbling. If velocity is $\omega \parallel \hat{z}$ (a non-tumbling state, since \hat{z} is a principal axis), then $\omega \parallel L$ and $\tau = \dot{L} \parallel \dot{\omega}$ so that ω remains parallel to \hat{z} and non-tumbling. These cases of torque are additionally significant because not as many terms contribute to τ_z as to τ_x and τ_y .

A4 Equations of motion

The equations of motion of the asteroid position D are given by Newton's law of gravitation:

$$\dot{V} = -\frac{G\mu_B}{D^3} D \quad \dot{D} = V \quad (\text{A12})$$

Rather than derive equations of motion for the Euler angles (which suffer from gimbal lock), we instead represent the orientation of the asteroid with a quaternion \tilde{q} which can be converted into Euler angles to compute $D(\alpha, \beta, \gamma)$. This quaternion evolves as

$$\dot{\tilde{q}} = \frac{1}{2}\tilde{q}\tilde{\omega}. \quad (\text{A13})$$

for angular velocity ω given in the body-fixed frame. The equations of motion of ω in turn are given by

$$\begin{aligned} I_x \dot{\omega}_1 - \omega_y \omega_z (I_y - I_z) &= \tau_x \\ I_y \dot{\omega}_2 - \omega_z \omega_x (I_z - I_x) &= \tau_y \\ I_z \dot{\omega}_3 - \omega_x \omega_y (I_x - I_y) &= \tau_z. \end{aligned} \quad (\text{A14})$$

Equations 4 to A14 form a set of non-linear, first-order coupled differential equations in which can be numerically integrated. They are expressed in terms of the constant physical parameters $\mu_{M/m}$, $a_{M/m}$, $J_{\ell m}$ and $K_{\ell m}$ given the density moment-moment of inertia relations given by equation 5.

Note that equation A14 is independent of a_A to first-order in τ , because $I_j \propto a_A^2$ for all j and $\tau \propto a_A^2$. Therefore,

scaling a_A merely scales the value of the sub-leading-order contributions to τ .

APPENDIX B: REFERENCE ASTEROID CONFIGURATIONS

Except when otherwise mentioned, we use the following asteroid encounter parameters. Many of the parameter choices are made to maximize the quality of observations (a close orbit, large asteroid, etc.) This is so that our uncertainties have room to grow; if the reference asteroid has low uncertainty, we would not be able to measure uncertainty increases as well when the encounter parameters are adjusted.

(i) An orbit around a spherical, Moonless Earth with 6 km s^{-1} excess velocity and perigee at 5 Earth radii. This orbit was chosen to roughly match that of 99942 Apophis [Giorgini et al. \(2005, 2008\)](#); [Smalley et al. \(2005\)](#), discovered on June 19, 2004 by R. A. Tucker, D. J. Tholen, and F. Bernardi. These orbital parameters correspond to an eccentricity of 3.88. The comparison to Apophis is complicated by the fact that Apophis is smaller than our a_A value, is tumbling [Pravec et al. \(2014\)](#), and may change slightly in physical properties due to tidal interaction during the encounter [Yu et al. \(2014\)](#); [Hirabayashi et al. \(2021\)](#). It therefore is not entirely comparable to our analysis.

(ii) An initial roll of $\gamma_0 = \pi/8$.

(iii) A cadence of 2 minutes and observational uncertainty of $\sigma_\theta = 0.01$ and $\sigma_\rho/\sigma_\theta = 10^{-5}$.

(iv) A rotational period of 9 hours, with the angular velocity vector distributed between the \hat{X} , \hat{Y} , and \hat{Z} axes in a $1 : 2 : -2$ ratio.

(v) An asteroid with radius $a_A = 1 \text{ km}$ and $K_{3m} = 0$. For K_{22} and K_{20} , we use two standard values: one with $(K_{22}, K_{20}) = (0, -0.097)$ and one with $(0.052, -0.202)$. Including the third point obtained by reflection $K_{22} \rightarrow -K_{22}$, these are the three points that minimize the mean distance between an arbitrary point in the allowed parameter space (equation A5) and these reference values. The first point is called the symmetric case because the corresponding uniform-density-ellipsoid model is rotationally symmetric around \hat{z} . The second case and its reflection are called the asymmetric cases. Values of $(0.052, -0.202)$ have $a < b$ in the ellipsoid model, and the reflected value has $a > b$. If not specified, we use the $a < b$ case. Specifically, the asymmetric case has $a = 1140 \text{ m}$, $b = 1839 \text{ m}$, and $c = 565 \text{ m}$, while the symmetric case has $a = b = 1411 \text{ m}$ and $c = 1008 \text{ m}$.

The surface of a spherical asteroid with this rotational period and a_A rotates at 25 cm s^{-1} at the equator. The asymmetric and symmetric ellipsoids have maximum equatorial velocities of 36 cm s^{-1} and 27 cm s^{-1} respectively.

We use the asymmetric ellipsoid in nearly all runs, due to the degeneracy induced in our model when $K_{22} = 0$.

APPENDIX C: ADDITIONAL DENSITY DISTRIBUTION MODELS

Two models were discussed in section 2.4 to translate density moment constraints into density distribution constraints.

Here we outline two additional models, the nearly-uniform and the harmonic models, which are less conventional but still useable for extracting density distribution properties. Unlike the finite element and lumpy models discussed in the main text, these models will yield smooth distributions with no discrete transitions. They also rely on a known surface for the asteroid.

C1 Nearly-uniform model

In this nearly-uniform model, we seek to pick one density distribution from the many distributions consistent with the data by maximizing a prior distribution $f[\rho(\mathbf{r})]$, which can be chosen manually. Any prior distribution can be chosen, but the following prior is both interesting and numerically efficient.

As part of our prior, we require that the asteroid density distribution satisfy $I_{\mathcal{A}} = \mu_{\mathcal{A}} a_{\mathcal{A}}^2$. This constraint is desirable as it encourages nearly uniform density distributions; recall that a perfectly uniform asteroid always satisfies this constraint. To define the prior, we divide the asteroid into $n \gg 1$ small regions of volume V , each with position \mathbf{r}_i and density $\rho_i = \delta_i + 1$. Setting the mass of the asteroid equal to its volume, the average density is 1, so δ_i is the difference between the average and local density. We set $f[\rho(\mathbf{r})]$ to be a multivariate-Gaussian distribution on δ_i centred on zero to minimize non-uniformity, i.e.

$$f[\rho(\mathbf{r})] \propto \prod_i \frac{\delta_i^2}{2\sigma^2} \quad (\text{C1})$$

where σ is an irrelevant constant. The density moments, MOI scale, and mass are

$$K_{\ell m} = \frac{V}{\mu_{\mathcal{A}} a_{\mathcal{A}}^\ell} \sum_i (\delta_i + 1) R_{\ell m}(\mathbf{r}_i) \quad (\text{C2})$$

$$I_{\mathcal{A}} = \mu_{\mathcal{A}} a_{\mathcal{A}}^2 = V \sum_i (\delta_i + 1) r_i^2 \quad (\text{C3})$$

$$\mu_{\mathcal{A}} = V \sum_i (\delta_i + 1) \implies 0 = \sum_i \delta_i. \quad (\text{C4})$$

Writing δ_i as an n -dimensional vector $\boldsymbol{\delta}$, equation C2 is a matrix equation for $K_{\ell m}$ and equations C3 and C4 are vector dot product equations. Combining $K_{\ell m}$, $I_{\mathcal{A}}$, and 0 into a single vector \mathbf{K} , these equations can be written as a single underdetermined matrix equation we denote as $\mathbf{K} = M\boldsymbol{\delta} + \mathbf{C}$, where the components of constant matrix M and constant vector \mathbf{C} are known given a fixed layout of the n regions. Some of the components of \mathbf{K} , such as $I_{\mathcal{A}}$, $\mu_{\mathcal{A}}$, and K_{1m} , are constraints. We treat the other components as parameters of the model. The task is then to find $\boldsymbol{\delta}$ that satisfies this matrix equation and minimizes $f(\boldsymbol{\delta}) \propto |\boldsymbol{\delta}|^2$. The Moore-Penrose inverse satisfies these properties:

$$\boldsymbol{\delta} = M^+(\mathbf{K} - \mathbf{C}); \quad M^+ = M^\dagger (MM^\dagger)^{-1} \quad (\text{C5})$$

where M^\dagger is the adjoint of M .

The probability distribution of \mathbf{K} is given by the output of the fit described in section 2.3. The parameters of this model, \mathbf{K} , might differ from this distribution due to the additional constraint that the density fall in realistic values.

This can be implemented by individually checking the components $\boldsymbol{\delta}$ computed by equation C5 and confirming that $1 + \delta_i$ lies within the acceptable range of densities.

C2 Harmonic model

For the harmonic model, we limit ourselves to density distributions that are harmonic; i.e., they satisfy $\nabla^2 \rho(\mathbf{r}) = 0$. We have no physical justification for why this assumption should be true, but it is useful as a simplification to gain qualitative insight into the properties of the asteroid density distribution.

A harmonic density distribution can be expanded in terms of the spherical harmonics as $\rho(\mathbf{r}) = \sum_{\ell m} C_{\ell m} R_{\ell m}(\mathbf{r})^*$ where $C_{\ell m}$ are complex, free parameters. This series can be truncated at some maximum ℓ . The density moments, MOI scale, and mass can then be explicitly computed as a function of $C_{\ell m}$:

$$K_{\ell m} = \frac{a_{\mathcal{A}}^{2-\ell}}{I_{\mathcal{A}}} \sum_{\ell m} C_{\ell' m'} \int_{\mathcal{A}} d^3 r R_{\ell' m'}(\mathbf{r})^* R_{\ell m}(\mathbf{r}) \quad (\text{C6})$$

$$I_{\mathcal{A}} = \sum_{\ell m} C_{\ell m} \int_{\mathcal{A}} d^3 r R_{\ell m}(\mathbf{r})^* r^2 \quad (\text{C7})$$

$$\mu_{\mathcal{A}} = \sum_{\ell m} C_{\ell m} \int_{\mathcal{A}} d^3 r R_{\ell m}(\mathbf{r})^*. \quad (\text{C8})$$

These integrals can be pre-computed given a known asteroid shape \mathcal{A} , so that computing $C_{\ell m}$ to match a given $K_{\ell m}$ is fast. Furthermore, their values when \mathcal{A} is spherical gives us insight into the influence of $K_{\ell m}$ on density distributions. In this case, $I_{\mathcal{A}} \propto C_{00}$ and the integral of equation C6 is nonzero only when $\ell' = \ell$ and $m' = m$. Therefore, $C_{\ell m}$ is proportional to $K_{\ell m}$. The density distribution can be immediately visualized given the density moments as a sum of the solid spherical harmonics weighted by $K_{\ell m}$. When the asteroid is non-spherical, the shape itself contributes to $K_{\ell m}$ so as to break this picture.

Imposing constraints on these moments is also necessary. The choice of mass is enforced merely by enforcing equation C8. We impose bounds on $\rho(\mathbf{r})$ by acknowledging that harmonic functions such as $\rho(\mathbf{r})$ in a region such as \mathcal{A} attain their maxima on the boundary of the region, so that it is only necessary to ensure that ρ lies within the allowed range on the asteroid boundary rather than within the entire asteroid. This can be done by parametrizing the asteroid surface as a function of two variables and minimizing and maximizing ρ with respect to those variables, ensuring these minima and maxima are within the allowed range.

APPENDIX D: THE CADENCE CUT-OFF

In section E4, we noted that posterior uncertainty as a function of observation cadence Δt appears to increase suddenly near $\Delta t \sim T_{\text{cad}} = 30 - 40$ min. In this appendix, we discuss the location of this cadence cut-off as a function of the physical parameters of the asteroid.

In figure D1, we display contour plots of posterior uncertainty $\sigma(K_{\ell m})$ of the fit parameters as a function of both cadence Δt and P_{ω} (left panel) or the relative orbit speed

$t_{\text{spin}}/t_{\text{orbit}}$ (right panel). Both panels show the same sudden increase in posterior uncertainty we named T_{cad} , located around the region where $\sigma_\rho/\rho = 100\%$ and now visible as a function of frequency and relative orbit speed. In all cases, the value of γ_0 was set so that all data points achieve the same value of γ at perigee.

Figure D1 demonstrates that large rotational period produces high T_{cad} . The dependence on P_ω agrees with the fact that large rotational periods for fixed cadence lead to better posterior uncertainty, discussed in section E7. The figure also demonstrates that for large P_ω , T_{cad} depends less strongly on P_{omega} and may even reverse its dependence such that increasing P_{omega} decreases T_{omega} . In all cases except $\Re K_{33}$, at least constant- $\sigma(K_{\ell m})$ contour is seen to curve back such that Δt decreases as a function of P_{omega} for large P_{omega} . In these regions the cadence cut-off also dulls, as shown by the spreading of the constant- $\sigma(K_{\ell m})$ contours in this region.

The relative orbit speed $t_{\text{spin}}/t_{\text{orbit}}$ was defined by unphysically increasing or decreasing the time at which the asteroid moved through the orbit determined by the equations of motion (but leaving the orbit shape unchanged). The equations of motion affecting the orientation and spin of the asteroid however were unaffected. $t_{\text{spin}}/t_{\text{orbit}} > 1$ corresponds to a faster orbit, and $t_{\text{spin}}/t_{\text{orbit}} < 1$ corresponds to a slower orbit. With this unphysical process, we isolate the effect of the amount of time spent near perigee on posterior uncertainty, without inheriting additional affects that would have been caused by the orbit changing shape.

The right panel of figure D1 shows a stronger and more monotonic dependence of T_{cad} on $t_{\text{spin}}/t_{\text{orbit}}$. It appears that even slightly slower orbits sharply increases T_{cad} . This effect is both due to the asteroid spending greater time in the high-torque, near-perigee region, and the larger data set that can be collected for slow orbits. However, if the orbit speed is changed by adjusting its parameters (v_∞, r_p) or the central body mass μ_B , then the orbit shape will also change. This induces other effects studied in the main text and will complicate the trend observed here. Unlike the P_ω case, the cadence cut-off does not visibly broaden as a function of $t_{\text{spin}}/t_{\text{orbit}}$. It appears that the increased orbit speed merely shifts T_{cad} rather than changing its sharpness.

APPENDIX E: UNCERTAINTY DEPENDENCE ON ENCOUNTER PROPERTIES

In this section, we investigate in greater detail the data presented in section 4.1 of the main text.

E1 Orbital elements

A Keplerian orbit is completely described by five parameters, but three describe the orbit's orientation with respect to the central body. They are therefore redundant with the orientation of the inertial frame and we do not investigate them here. We parametrize the remaining two parameters by the perigee distance r_p and excess velocity v_∞ . Fits of the type described in section 2.3 were run for many values of r_p and v_∞ and the 1 and 2σ posterior uncertainties are displayed in figure 9.

Figure 9 demonstrates that posterior uncertainty follows a slight trend for uncertainty to increase with v_∞ . This is likely due to the fact that larger v_∞ leads to a faster and flatter orbit with less time spent close to the planet, where tidal torque is strongest. There are also comparatively large oscillations in the uncertainty, due to the orientation of the asteroid at perigee varying. (The asteroid is always simulated to start at the same orientation, but increasing v_∞ decreases the time to perigee so that the asteroid enters this region of high torque at different orientations depending on v_∞ .) Hence, the oscillations have the same period for all parameters. The dependence of posterior uncertainty on v_∞ is weak enough so that σ_ρ/ρ never reaches 100% for the v_∞ investigated.

The figure shows much stronger dependence of parameter uncertainty on perigee distance, as expected by the factor of $(a_A/D)^{\ell'}$ present in equation 4 and mentioned in section A3. For $r_p = 7.9$ Earth radii, σ_ρ/ρ reaches the 100% threshold. The 20% threshold is reached at lower 4.7 Earth radii. Much of this uncertainty is dominated by uncertainty in K_{30} , which is the parameter least constrained by tidal torque analysis. At $r_p \approx 10$ Earth radii, K_{30} fills the prior distribution with uncertainty ranging from -1 to 1, visible by the sudden cut-off in uncertainty increase and the discontinuity of the $\sigma(K_{\ell m})$ curve there.

The axes of figure 9 show that parameters with large m are more precisely determined than parameters with small m , as can be seen by comparing K_{22} to K_{20} and comparing K_{33} to other K_{3m} values. Large m moments correspond to moments that control higher frequency fluctuations in density at the asteroid equator. This pattern of $\sigma(K_{\ell m})$ smaller for large m is a general trend and will be seen in the following sections as well.

The very strong dependence of $\sigma(K_{\ell m})$ on r_p makes this analysis most useful to extract second-order moments on close encounters. Fortunately, in the case of Earth, these encounters are also likely to have the best associated observational uncertainty when above the horizon due to their proximity. The first-order moments can still be extracted at much larger perigee distances in our model.

E2 Observational uncertainty

Two parameters, σ_θ and σ_ρ , govern the observational uncertainty of the data set. These parameters are defined in section 2.2; σ_θ represents the standard deviation of the angle between the true spin pole and the observed spin pole, while σ_ρ represents the standard deviation of the ratio between the observed and true rotational velocities. Rather than explore the full space spanned by these two values, we fix one and allow the other to vary to better assess whether uncertainty in spin pole or uncertainty in period more strongly affects posterior uncertainty $\sigma(K_{\ell m})$. This dependence is displayed in figure 9.

For the case in which σ_ρ is held fixed and σ_θ is varied, the figure shows that the dependence of $\sigma(K_{\ell m})$ on σ_θ is linear. The uncertainty threshold is reached at $\sigma_\theta = 2.8^\circ$ (0.5°) for $\sigma_\rho/\rho = 100\%$ (20%). The K_{2m} uncertainties remain low, even for $\sigma_\theta \approx 1$, which is large enough that the spin pole has non-negligible probability to be observed in any direction.

If σ_ρ is allowed to vary instead, then K_{30} reaches the

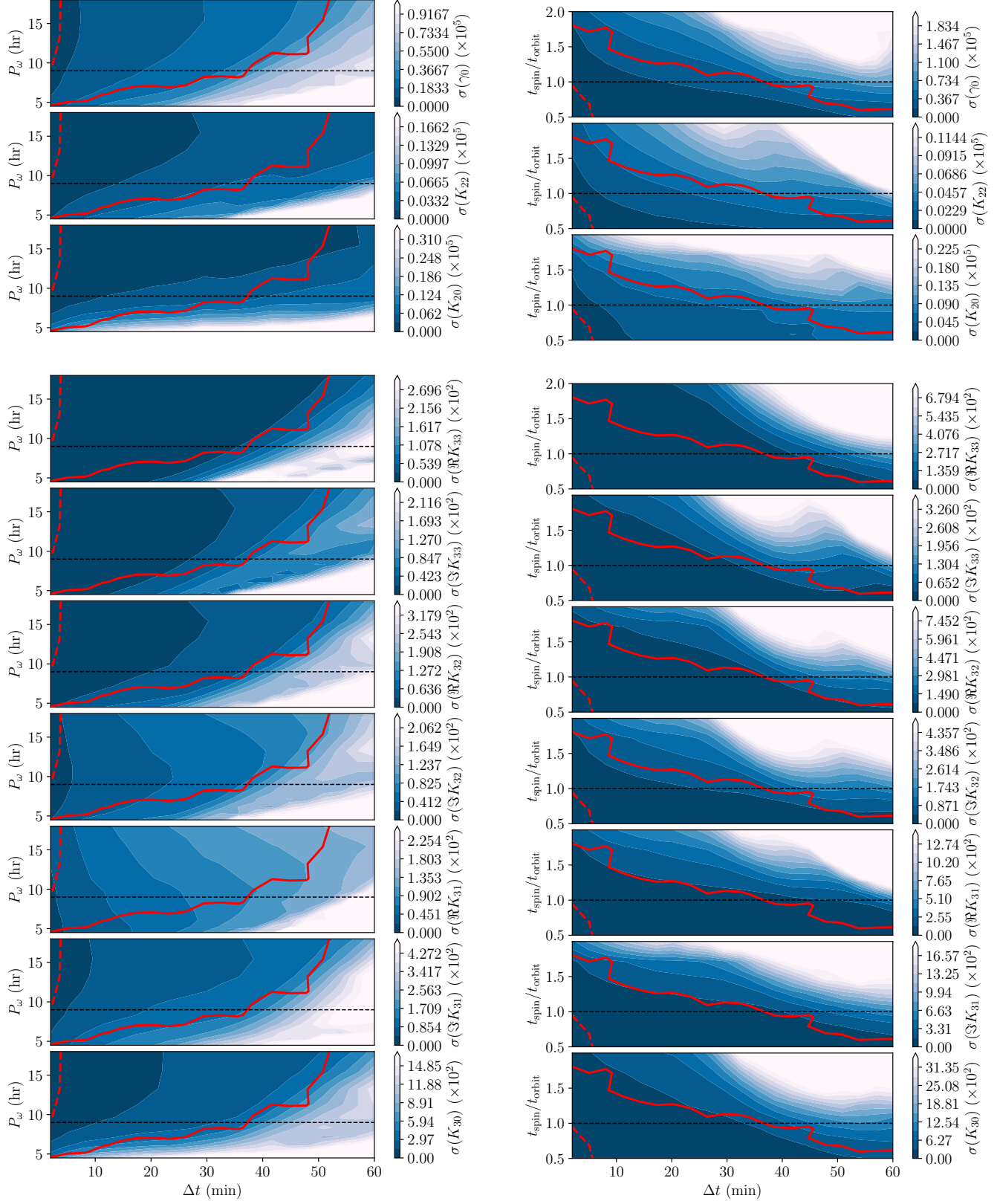


Figure D1. Contour plots showing posterior uncertainties as a function of cadence Δt and dynamical time scales for the encounter: rotational period P_ω (left) and the relative speed of the orbit (right; see text for a definition). The reference values of $P_\omega = 9$ hr and $t_{\text{spin}}/t_{\text{orbit}} = 1$ are shown as dotted lines. The solid (dotted) red line represents the $\sigma_\rho/\rho = 100\%$ (20%) threshold. Cadence cut-off depends strongly on both P_ω and $t_{\text{spin}}/t_{\text{orbit}} = 1$.

100% and 20% thresholds at σ_ρ which correspond to period uncertainty of several milliseconds. At large period uncertainty, the PPDs begin to fill the prior and the posterior uncertainty $\sigma(K_{\ell m})$ is no longer linear with σ_ρ (this is especially visible in the K_{30}) case. Otherwise, posterior uncertainty is proportional to σ_ρ .

These data show that posterior uncertainty is extremely sensitive to observational uncertainty in period in our analysis. To precisely measure density moments, very accurate rotational period estimates would have to be made for every angular velocity data point. However this analysis does not study the effect of collecting more data after the encounter, or the correlations between different angular velocity measurements. If these correlations were taken into account, or a more accurate uncertainty model used which took into account the asteroid's location in the sky or its distance to Earth, then the precision limit we find here will be affected.

E3 Asteroid shape

The true values of $K_{\ell m}$ and a_A , which quantify the asteroid's physical properties, affect the posterior uncertainties. Here, we only investigate the sensitivity of $\sigma(K_{\ell m})$ to the first-order parameters and a_A . These K_{2m} moments can also be viewed as the axes of a uniform density triaxial ellipsoid (equation A4).

In figure 7, we show the 1σ posterior uncertainties as a function of K_{20} and K_{22} , or alternatively a/c and b/c . We use axis ratios rather than the values of a , b , and c because axis ratios are independent of a_A . The large $|K_{22}|$ sides of the K_{2m} -space plots correspond to asymmetric ellipsoids, as do the points far from the $a/c = b/c$ diagonal of the axis-ratio-space plots. The point corresponding to a sphere, which experiences no tidal torque and no tumbling, is at $K_{2m} = 0$ and $a/c = b/c = 1$.

The figure shows large uncertainty in γ_0 for $K_{22} = 0$, or $a/c = b/c$, because K_{20} is rotationally symmetric around \hat{z} , and γ_0 is the initial orientation with respect to the \hat{z} axis. The system then has no dependence on γ_0 when $K_{22} = 0$. This induces degeneracy in the model which inflates uncertainties, not only in γ_0 but also the other components.

To remove the inflated uncertainty, one could assume a rotationally symmetric asteroid, remove γ_0 as a parameter, and run a fit. For a nearly rotationally symmetric asteroid however, a new parametrization is necessary which does not contain the ill-constrained γ_0 parameter. This task is beyond the scope of this paper, so we mostly consider asymmetric asteroids throughout.

Figure 7 also shows low uncertainty for highly asymmetric asteroids, where b/c and a/c are very different (i.e., when $|K_{22}|$ is large). Additionally, $\sigma(K_{20})$ and $\sigma(K_{22})$ decrease for large $|K_{20}|$, which corresponds to large axis ratios in the ellipsoid case.

Figure E1 displays the correlation between the first-order parameters. They show that γ_0 and K_{22} are often correlated for asymmetric asteroids, while γ_0 and K_{20} are usually not. This is expected as K_{22} is dependent on the orientation of the asteroid and K_{20} is not. They also show that K_{22} and K_{20} are usually correlated, and that a/c and b/c are highly correlated. The latter is expected due to the $1/c$ dependence.

The fact that $K_{\ell m}$ are correlated indicates that, in or-

der to correctly propagate density moment uncertainties to a density distribution, a full PPD is necessary. If only 1σ uncertainty intervals for each parameter were used, density distribution uncertainty would be overestimated. This full PPD is produced by our fit process, but only the 1σ uncertainties are displayed in this paper in most cases.

Overall, the variation in the uncertainties on K_{20} and K_{22} (the first-order density moments) is present but largely smooth across their allowed parameter space, as is their correlation. It therefore seems reasonable to use the asymmetric asteroid shape as a stand-in for an unknown's asteroid shape when simulating an encounter, as we do in this paper. The uncertainty then can be expected to differ across other shapes by a factor of about two or less, as long as the degenerate, symmetric asteroid regime is avoided.

On the other hand, the posterior uncertainty of K_{3m} is much more strongly dependent on asteroid length a_A . Figure 10 displays posterior uncertainty $\sigma(K_{\ell m})$ as a function of a_A . As was mentioned in section A3, the K_{2m} parameters are insensitive to a_A since the a_A^2 term in τ (equation 4) cancels the a_A^2 in the MOI (equation 5). The K_{3m} uncertainty is strongly dependent on a_A for the same reason that it is dependent on r_p : the $(a_A/D)^{\ell'}$ dependence of equation 4. At $a_A \leq 1100$ m, $\sigma_\rho/\rho \approx 100\%$. However, the 20% cut-off is much lower, at $a_A \leq 180$. Figure 10 demonstrates why these cut-offs are so distant; for large a_A , uncertainty decreases slowly with length. Only for small lengths is the uncertainty very large. This behaviour indicates that the uncertainty threshold is unlikely to fall much below 180 m even if other properties of the encounter are adjusted.

For uniform density asteroids, large a_A is equivalent to large asteroid radius. In non-uniform density asteroids, large a_A can also be achieved by distributing the mass of the asteroid near the surface, because the r^2 term in the integrand of the definition of a_A causes the density of regions distant from the asteroid centre of mass to dominate a_A .

E4 Cadence

The time between observations of asteroid angular velocity, or cadence, may vary depending on the observational schedule of the observing telescopes and the path of the asteroid through the sky. We measure how the posterior uncertainty $\sigma(K_{\ell m})$ varies with cadence ranging from two minutes to one hour in figure 10.

Figure 10 displays little dependence of uncertainty on cadence Δt for $\Delta t \lesssim 40$ min. We also see flaring of uncertainty for very large cadence, largely driven by the paucity of data points. However, uncertainty dramatically increases for many parameters at about $\Delta t = 30 - 40$ min, a time scale which is likely characteristic of the asteroid system. We name this rough cadence limit T_{cad} . T_{cad} is also the location at which the $\sigma(K_{3m})$ threshold is crossed for all second-order moments except K_{30} , which exceeds the uncertainty threshold at $\Delta t \approx 5$ min.

We expect this T_{cad} to be a function of two dynamical time scales of the system: the rotational period of the asteroid P_ω and the dynamical time scale of the orbit (the latter can be estimated in multiple ways, since both r_p/v_∞ and $v_\infty r_p^2/\mu_B$ have units of time and may be relevant). How these time scales affect T_{cad} is discussed in appendix D.

Figure 10 shows that as long as $\Delta t < T_{\text{cad}}$ is achieved,

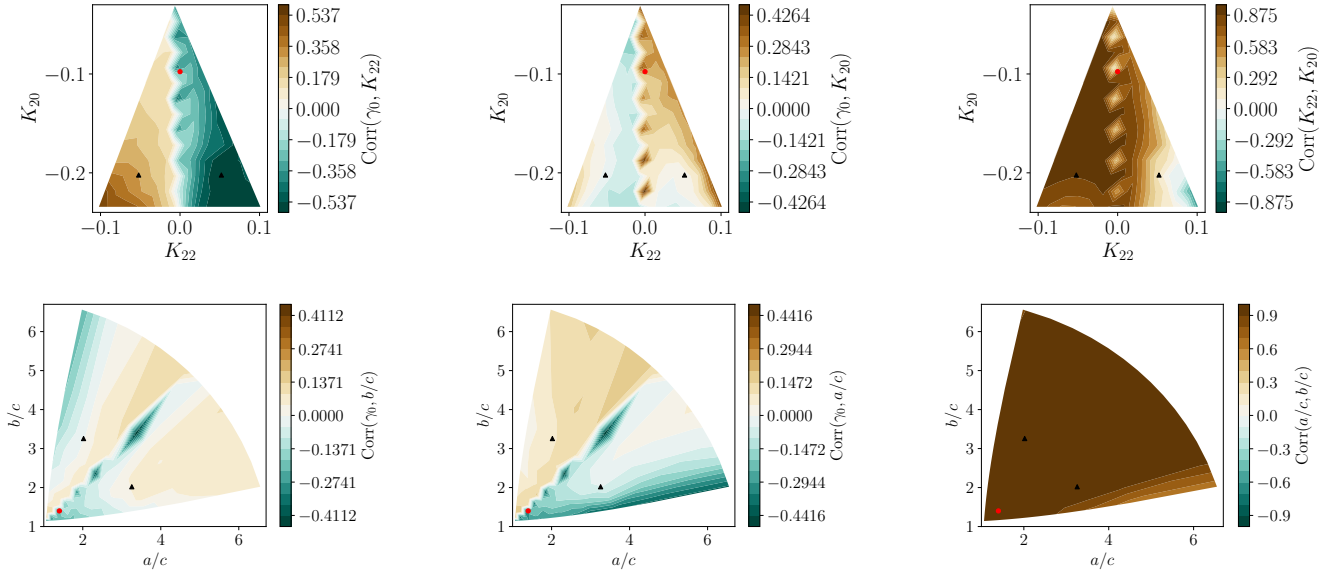


Figure E1. Correlations between PPDs for first-order parameters γ_0 , K_{22} , and K_{20} (top row) and γ_0 , a/c , and b/c (bottom row). Also shown as black points are the reference asteroid shapes: symmetric (red circle) and asymmetric (black triangle). The first order parameters K_{22} and K_{20} are correlated, as are initial orientation γ_0 and K_{22} .

the influence of cadence on σ is minimal, but shorter cadence leads to lower uncertainties.

E5 Perigee gap

In certain circumstances, spin data might not be able to be captured for a close encounter at perigee. The asteroid might dip below the horizon, or it might pass too close to the sun to be observed. Generally, angular velocity data can be collected when the asteroid is distant from the central body, where torque is low. There, the angular velocity evolution is dominated by torque-free precession dictated by the MOI components. That zero-torque data can still be used to fix K_{20} and K_{22} as in Moskovitz et al. (2020). However, K_{3m} does not affect the precession periods (though they do affect the phase). We are therefore curious as to how our posterior uncertainties change due to lack of perigee data.

To test this, we mask the perigee of the counter by removing a duration T_{gap} of data centred on the perigee, where T_{gap} ranges from 0 to 3 hours. To prevent lack of precision on $K_{\ell m}$ induced by lower amounts of data for high T_{gap} , we always cut 3 hr – T_{gap} from the data set, half from the beginning and half from the end, so that each data set produced for all T_{gap} has the same size. We then fit the same asteroid model to the cut data for all T_{gap} and plot posterior uncertainties $\sigma(K_{\ell m})$ in figure 10.

Since torque is greatest at perigee, we expect that region of the data to contain the most information about $K_{\ell m}$, and therefore uncertainty should increase monotonically with T_{gap} , which is seen in figure 10. We also see that the first-order parameters are not as sensitive to T_{gap} as the second-order parameters, because K_{2m} are additionally constrained by torque-free precession after perigee.

Most parameters show dramatically increased uncertainty in the $T \sim 1 - 2$ hr range. On the other hand, none of the uncertainties increase noticeably for $T \lesssim 1$ hr. Thirty

minutes of dropped data is equivalent to fifteen dropped points for the simulated cadence of $\Delta t = 2$ minutes, showing that many data points can be dropped from the data set at perigee before the uncertainty starts to increase.

Qualitatively, 10 shows similar dependence of $\sigma(K_{\ell m})$ on T_{gap} as on cadence Δt ; they also both have cut-offs where uncertainty markedly increases, and both the T_{gap} and Δt cut-offs have qualitatively similar shapes although they occur at different values of Δt and T_{gap} . This suggests that the factors that govern uncertainty due to cadence also may govern sensitivity to lack of data at perigee in a similar way.

E6 Initial spin pole

The tidal torque experienced by the asteroid is affected by the initial direction of asteroid spin Ω_0 both because spin sets the initial asteroid orientation up to γ_0 and because of the spin-dependence of the rotational equations of motion (equation A14).

In figure 8, we display 1σ posterior uncertainties as a function of the direction of Ω_0 mapped onto the unit sphere in the inertial frame. Our samples for Ω_0 were laid out on a Fibonacci sphere to ensure they were roughly evenly spaced (marked in figure E2). To highlight common features across the parameters, we also display the average 1σ sensitivity in figure E2. The average is weighted such that the uncertainty map for each parameter contributes an equal amount (the weight of each map is set to one-tenth of the map's mean). This average map is presented in two different projections to allow data at \hat{Z} to be read.

Certain alignments of the body-fixed frame to the inertial frame lead to special conditions on torque, as discussed in section A3. For example, $z \parallel \hat{Z}$ and $z \parallel \hat{Y}$ at perigee lead to $\tau \parallel \hat{z}$ to first-order, and $\tau \parallel \hat{X}$ at perigee leads to $\tau = 0$ to first-order. We relate this to the initial direction of Ω_0 , via the approximation that τ is small until perigee. Then

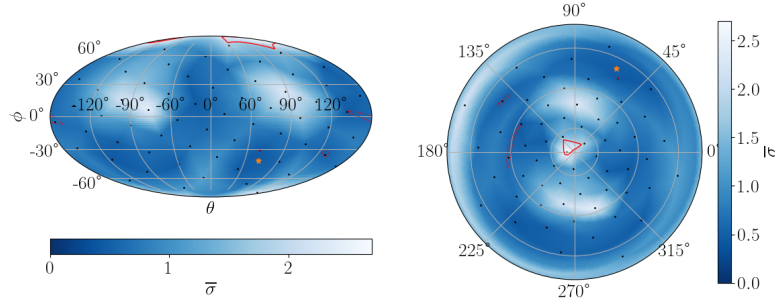


Figure E2. The weighted average of the uncertainties shown in figure 8, in Mollweide (*left*) and polar (*right*) projections in the inertial frame. See text for a description of how the average was computed. Black dots indicate the Fibonacci-sphere-distributed locations of sample spin poles, and the orange star indicates the reference spin pole. The polar projection is centred at the north pole, or $\hat{\mathbf{Z}}$. Posterior uncertainty is large near $\pm\hat{\mathbf{Z}}$ and $\pm\hat{\mathbf{Y}}$, but roughly constant elsewhere.

$\Omega_0 \parallel \hat{\mathbf{Y}}$ and $\Omega_0 \parallel \hat{\mathbf{Z}}$ both lead to $\tau \parallel \hat{\mathbf{z}}$, and $\Omega_0 \parallel \hat{\mathbf{X}}$ leads to $\tau = 0$.

Figure E2 shows area of increased uncertainty for $\Omega_0 \parallel \hat{\mathbf{Z}}$ and $\Omega_0 \parallel \hat{\mathbf{Y}}$, but not the $\hat{\mathbf{X}}$ case. This indicates that $\tau \parallel \hat{\mathbf{z}}$ causes increased uncertainty. Physically, $\tau \parallel \hat{\mathbf{z}}$ only changes an asteroid's rotational period and does not cause it to tumble, eliminating the ability to discern MOI ratios from zero-torque precession after the encounter. If $\tau = 0$ to first-order, then second-order τ and non-perigee τ will dominate, which may increase precision to these usually non-dominant parameters and therefore not have the same increasing effect on $\sigma(K_{\ell m})$.

However, uncertainty does not vary by much more than a factor of two outside the imprecise regions of $\Omega_0 \parallel \hat{\mathbf{Z}}$ and $\Omega_0 \parallel \hat{\mathbf{Y}}$, though these regions are wide for some parameters. Within the imprecise regions, uncertainty can grow up to four times or more the uncertainty at other Ω_0 values, and can exceed the $\sigma(K_{3m}) \approx 0.01$ threshold. The trends for are roughly consistent across parameters (figure 8), leading to clearly visible imprecise regions in the average $\sigma(K_{\ell m})$ (figure E2).

E7 Rotational period

We also study the effect of the initial rotational period of the asteroid P_ω on posterior uncertainty $\sigma(K_{\ell m})$. In figure 10, we show $\sigma(K_{\ell m})$ as a function of P_ω for a range of periods typical of NEOs. Like figure 9, depicting the dependence of $\sigma(K_{\ell m})$ on v_∞ , figure 10 shows small-scale variation in uncertainty due to the fact that varying the initial period changes the value of γ at perigee, which affects uncertainty to a factor of about two. But a large-scale trend is also visible in many parameters. K_{20} and K_{22} show very large uncertainty for $P_\omega \lesssim 4$ hr because these fast-rotators tumble very little after perigee. This increases uncertainty on the K_{2m} parameters, which are constrained by tumbling.

We expect that quickly rotating asteroids would not tumble because, for small P_ω , the dynamical variables \mathbf{D} , $\boldsymbol{\omega}$, α , and β vary much smaller than γ . Approximating each variable as constant over one full rotation of $\gamma \in (0, 2\pi)$, we can integrate the first-order contribution of τ over $\gamma \in (0, 2\pi)$, which gives no secular, first-order torque to force the asteroid to tumble. However, this effect does not apply to the second-

order parameters, since the integral over the second-order term of τ does not vanish, as seen in the figure.

Another feature of figure 10 is that $K_{\ell 0}$ is more uncertain at low P_ω than the other parameters. This is most visible in the figure for K_{30} . The cause is likely that $K_{\ell 0}$ cannot contribute to τ_z as shown in equation 4. We already discussed that asteroids with small P_ω do not tumble, and since τ_x and τ_y are what induces tumbling, the most observable component of torque is therefore τ_z , which $K_{\ell 0}$ do not affect.

The most severe effect of period on $\sigma(K_{\ell m})$ is in the low-period regime ($P_\omega < 4.3$ hr), but in this case, the most strongly affected parameters are K_{2m} , which are generally known better than K_{3m} . The effect on the imprecise parameters K_{3m} is small, except for K_{30} . It therefore seems as though small-period asteroids are still candidates for observation, although high-period asteroids yield smaller uncertainty.

E8 Central body oblateness

In all the above studies, we assumed a spherical planet ($J_{\ell m} = 0$ for $\ell \geq 1$). By assumption that $\mu_B \gg \mu_A$ (so that the asteroid orbit's focus is the centre of mass of the central body), we have $J_{1m} = 0$. The effect of central body non-sphericity, then, is limited to the J_{2m} terms and damped by a factor of $(a_B/D)^2$. We expect these parameters to have small effect on the asteroid.

Here, we define oblateness as $\epsilon = (I_z - I_x)/(\mu_B R_B^2)$, where $I_{x,y,z}$ are the central body moments of inertia along the principal axes, and $I_x = I_y$. R_B is the true radius of the body (not a_B from equation A3).

$J_{\ell m}$ is defined in equation A3 with respect to the asteroid orbit, not the principal axes of the central body. However, for an equatorial orbit, the central body principal axes coincide with the asteroid orbit frame and we may express ϵ simply in terms of $J_{\ell m}$ as $\epsilon = -10J_{20}/3$ and $J_{22} = 0$. For simplicity, we use this equatorial orbit case. Since an oblate ellipsoid is mirror-symmetric around all three axes, table A1 indicates that J_{3m} are all zero. The next order of tidal torque is therefore J_{4m} , damped by an additional $(a_B/D)^2$ factor, and non-ellipsoid corrections to the central body shape. We do not consider these extra factors.

Given this conversion between ϵ and J_{20} , we analyze

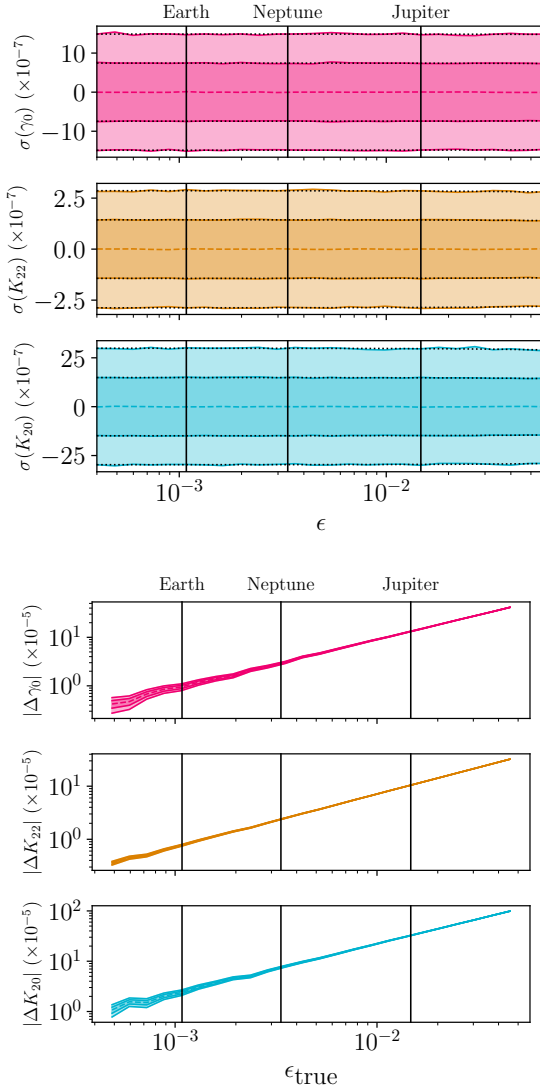


Figure E3. Top: 1 and 2σ confidence intervals for the first-order parameter PPDs as a function of oblateness ϵ . Linear best-fitting lines to $\sigma(K_{2m})$ (black, dotted) are plotted. Bottom: The difference between PPD means extracted from a zero-oblateness model and the true parameters given data with true oblateness $\epsilon_{\text{true}} \neq 0$. Also shown in both figures are the oblatenesses of reference Solar System bodies. Posterior uncertainty depends little on oblateness, but the best-fitting parameter estimates are affected enough by oblateness that oblateness must still be modelled.

posterior uncertainty $\sigma(K_{2m})$ of the first-order parameters as a function of ϵ across a reasonable range of central body oblatenesses based on those of Solar System planets Pater & Lissauer (2015). These uncertainties are shown in the top panel of figure E3, together with linear best-fitting curves. The figure demonstrates almost no dependence of $\sigma(K_{\ell m})$ on oblateness ϵ , although posterior uncertainty does measurably decrease for oblate central bodies. The best-fitting lines match the uncertainties well, and they have slope of $[\Delta\sigma(K_{\ell m})/\sigma(K_{\ell m})]_{\epsilon=0}/\Delta\epsilon = -0.06$ for γ_0 , -0.2 for K_{22} , and -0.3 for K_{20} . The second-order parameters K_{3m} likely depend on oblateness similarly, but fitting these parame-

ters is computationally more expensive and we do not study them.

Note that if an encounter is executed around one of the non-Earth objects noted in figure E3, a_B and μ_B will change in addition to ϵ . These two parameters also affect the posterior uncertainty (section 4.2), so the figure does not show that encounters with other bodies have the same precision as encounters with Earth; only that the difference in oblateness between the two bodies is of little concern.

Given the small effect of ϵ on $K_{\ell m}$, it might be tempting to neglect the planetary oblateness when fitting $K_{\ell m}$ to data. However, the bottom panel of figure E3 demonstrates that doing so is invalid. This figure displays $K_{\ell m}$ as extracted by a fit assuming $\epsilon = 0$, but run on data generated with non-zero ϵ . The difference between the PPD means and true parameters are shown. Posterior uncertainties are also shown as bands. The figure shows that even for low (Earth-scale) oblateness, the fit results are inconsistent with the true $K_{\ell m}$ values, since $\Delta K_{\ell m} = 0$ is not contained in the 2σ band. This effect is much worse for large oblateness, growing to a difference on the order of $\mathcal{O}(100)\sigma$ for Jupiter's oblateness. Therefore, accurately modelling central-body oblateness to high precision is essential for accurate estimation of fit parameters. For non-equatorial orbits, with $J_{22} \neq 0$, we also expect J_{22} to affect the accuracy of the fit results to a similar degree, with the additional requirement of using the correct asteroid orbital plane.

J_{20} , the parameter studied in this section, has a slightly more general definition than oblateness. If the planet has a moon, the integral defining J_{20} (equation A3) can be extended to include this extra mass, though this can only be done when the asteroid never passes inside the moon's orbit. As an order-of-magnitude estimate for this effect, two spherical objects with masses and radii of Earth and the Moon, separated by one Lunar distance, and both lying in the orbital plane has a combined oblateness of $\epsilon = 0.82$. Extrapolating posterior uncertainties via the slopes of the best fit lines given earlier yields a reduction in $\sigma(K_{2m})$ by about 25%. Furthermore, J_{22} is non-zero for this case, which likely decreases posterior uncertainty even more.

This analysis suggests that large moons such as ours can improve fit quality, but further study of this effect is beyond the scope of this paper. Without a moon to inflate the oblateness of the central body, planetary oblateness does not significantly improve posterior uncertainty. However, correct representation of oblateness is essential to accurately estimate $K_{\ell m}$.

This paper has been typeset from a TeX/LaTeX file prepared by the author.